ARTICLE IN PRESS

Palaeogeography, Palaeoclimatology, Palaeoecology xxx (xxxx) xxxx



Contents lists available at ScienceDirect

Palaeogeography, Palaeoclimatology, Palaeoecology

journal homepage: www.elsevier.com/locate/palaeo



Phytoliths, pollen, and microcharcoal from the Baringo Basin, Kenya reveal savanna dynamics during the Plio-Pleistocene transition

Chad L. Yost^{a,*}, Sarah J. Ivory^b, Alan L. Deino^c, Nathan M. Rabideaux^d, John D. Kingston^e, Andrew S. Cohen^a

- ^a Department of Geosciences, University of Arizona, 1040 E 4th St., Tucson, AZ 85721, USA
- ^b Department of Geosciences, Pennsylvania State University, State College, PA 16801, USA
- ^c Berkeley Geochronology Center, 2455 Ridge Road, Berkeley, CA 94709, USA
- ^d Department of Chemistry, Rutgers University-Newark, Newark, NJ 07109, USA
- ^e Department of Anthropology, University of Michigan, 1085 S. University Avenue, Ann Arbor, MI 48109, USA

ARTICLE INFO

Keywords: Microfossils Paleofire Mid-Piacenzian Warm Period Northern Hemisphere glaciation Tugen Hills Hominins

ABSTRACT

As part of the Hominin Sites and Paleolakes Drilling Project (HSPDP), phytoliths, pollen, and microcharcoal were examined from the 228 m (3.29 to 2.56 Ma) Baringo-Tugen Hills-Barsemoi drill core (BTB13). A total of 652 samples were collected at ~10 to 32 cm intervals, corresponding to sub-millennial to millennial scale temporal resolution. Microcharcoal was well-preserved throughout the core and often peaked in abundance ~5 kyr before and after insolation peaks. Phytolith preservation varied between excellent to total dissolution in alternating intervals throughout the core. Pollen was rarely preserved. These combined datasets indicate that prior to ~3.1 Ma, woody cover fluctuated between open savanna (< 40% cover), woodland (40–80% cover), and forest (> 80% cover) at typically precessional (19-23 kyr) periodicities. During the mid-Piacenzian Warm Period (MPWP; 3.26-3.01 Ma), intervals with exceptionally high microcharcoal abundance suggest that regional turnover from wooded to open habitats was driven in part by fire. After ~3.1 Ma, low-elevation woody cover likely never exceeded 40%, with oscillations between mesic tall-grass vs. xeric short-grass savanna at precessional periodicities. Mesic C4 tall-grass (Panicoideae) peaked in abundance during insolation maxima, whereas xeric C₄ short-grass (Chloridoideae) peaked during insolation minima. The onset of Northern Hemisphere glaciation (NHG) at ~2.75 Ma coincided with the appearance of deep lake phases and increases in grass density and fire frequency. Spectral analysis and intervals with well-preserved phytoliths indicate that precession and interhemispheric insolation gradients influenced vegetation via their effects on equatorial precipitation and fire. This study fills a crucial gap in Pliocene vegetation reconstructions from the East African Rift Valley and its associated hominin localities. It also provides orbitally resolved regional vegetation data useful in paleodatamodel comparisons for the onset of the MPWP (which is often used as an analog for future warming) and NHG.

1. Introduction

Late Neogene geological sections from the Baringo Basin and Tugen Hills area of the central Kenya Rift Valley have been the focus of intensive paleoenvironmental and paleoanthropological investigations for the past several decades (Pickford et al., 1983; Hill, 1985; Hill et al., 1992; Hill, 2002; Jacobs, 2002; Kingston et al., 2002; Deino et al., 2006; Kingston et al., 2007). The Hominin Sites and Paleolakes Drilling Project (HSPDP) targeted the Plio-Pleistocene fluviolacustrine deposits of the Chemeron Formation in the Tugen Hills, Kenya, as one of six East African drill sites with high potential to reveal linkages between environmental change and human evolution (Cohen et al., 2016). The

Chemeron Formation contains over 100 fossil vertebrate localities, including several hominin sites, three of which are located within 3 km of the HSPDP drill site and within the time interval encompassed by the drill core (Deino and Hill, 2002; Deino et al., 2002; Campisano et al., 2017).

Various hominin-environment models such as the *Savanna Hypothesis* (Bender et al., 2012) and the *Variability Selection Hypothesis* (Potts, 1998) have been proposed to explain possible environmental drivers of hominin evolution. Variables such as precipitation, Earth orbital parameters, and tectonics (rifting and volcanism) are often invoked in these evolutionary models. However, it has been argued that regardless of the specific selection mode that was operative, ultimately

* Corresponding author.

E-mail address: chadyost@email.arizona.edu (C.L. Yost).

https://doi.org/10.1016/j.palaeo.2020.109779

Received 20 March 2019; Received in revised form 27 April 2020; Accepted 27 April 2020 0031-0182/ © 2020 Elsevier B.V. All rights reserved.

it is the availability of water (Cuthbert and Ashley, 2014; Cuthbert et al., 2017) and the structure and composition of vegetation (Barboni et al., 2019) that are critically important for hominin survival. These aspects of landscape architecture support faunal populations and set the framework for predator-prey relationships, species/functional group competition/facilitation, and dispersal into novel environments (Potts, 2004; Kingston, 2007; Wells and Stock, 2007; Bunn and Gurtov, 2014).

Almost four decades ago, Hill (1981) called for the explicit inclusion of paleoecology into discussions on the evolution of human morphological change. However, vegetation-based paleoecological data at the appropriate taxonomic resolution from the basins where hominins lived were scattered and discontinuous across the Plio-Pleistocene (Bonnefille, 2010; Jacobs et al., 2010; Barboni, 2014). Several studies have recently produced such datasets (e.g., Novello et al., 2015; Arráiz et al., 2017; Novello et al., 2017; Albert et al., 2018; Ivory et al., 2018; Owen et al., 2018), yet there remains a paucity of paleovegetation records. This is especially true for records from the Plio-Pleistocene transition that show vegetation dynamics at time scales relevant to issues of hominin adaptation to abrupt vegetation change and high-frequency variability (Campisano et al., 2017).

To specifically address this shortcoming, we use direct paleoecological evidence primarily from phytoliths and microcharcoal, complemented with pollen data where preserved, to reconstruct fire and vegetation dynamics in the Baringo Basin at millennial to sub-millennial scales from the Baringo-Tugen Hills-Barsemoi HSPDP drill core (BTB13), which spans 3.29 to 2.56 Ma. This interval captures the mid-Piacenzian Warm Period (MPWP) and the subsequent initiation of global cooling, the onset of Northern Hemisphere glaciation (NHG), the diversification of *Paranthropus* and *Homo*, and the earliest evidence for stone tools (Harmand et al., 2015). With 652 samples analyzed from a 228-m core spanning 730 kyr, this record represents one of the most extensive phytolith studies ever conducted.

2. Background

2.1. Phytoliths from lake sediments

Phytoliths are microscopic opal silica ($SiO_2 \cdot nH_2O$: opal-A) infillings and casts of plant cells (Piperno, 2006; Strömberg et al., 2018). When plant material decays or is burned, phytoliths persist and are incorporated into soils and sediments. Phytoliths are transported to lake sediments by sheet-wash, fluvial, and eolian processes while still embedded in fresh or burned plant fragments, or after in situ plant matter decays (Yost et al., 2013; Aleman et al., 2014). Phytolith assemblages for lakes surrounded by moderate to high relief landscapes, such as rift settings, are assumed to reflect a weighted average of the lake catchment vegetation mosaic, with individual phytoliths capable of being transported up to 10^4 m (Yost et al., 2018; Li et al., 2019).

2.2. The use of grass subfamily phytolith indicators

Grass pollen can rarely be identified below the family level, and stable carbon isotopic approaches cannot distinguish C₃ grasses from all other C₃ plants, thus the diversity and habitat specificity of grasses has not been fully exploited in paleoecology. A major strength of phytolith analysis is the ability to identify grasses, with some degree of certainty, to subfamily and sometimes lower taxonomic levels, for which there are often significant differences in photosynthetic fixation of carbon (C₃, C₄ NADP-ME, C₄ NAD-ME and PCK), moisture, temperature, and light requirements. Issues with phytolith morphotype multiplicity and redundancy (Barboni and Bremond, 2009; Neumann et al., 2017) are overcome when considering the dominant association of particular phytolith morphotypes at various taxonomic and functional type levels, and considering the fact that a small number of grass species comprise the majority of the biomass in many grass-dominated systems (Edwards et al., 2010). For example, there are 200 grass species in the Serengeti

(Williams et al., 2016), but only 10 to 15 species are common, and often only two or three species dominate a given grass community (Belsky, 1983, 1985, 1986; Banyikwa et al., 1990).

2.3. Short-grass vs. tall-grass savanna

The short-grass/tall-grass boundary is a significant, but underappreciated ecological division in paleoecology. By extension, an underutilized paleoecological tool is the Iph phytolith index, which can differentiate between short-grass and tall-grass savannas (Bremond et al., 2008; Novello et al., 2017). Short-grass savannas are dominated by Chloridoideae grasses, and their abundance is negatively correlated with precipitation (Taub, 2000). Tall-grass savannas are dominated by Panicoideae grasses, whose abundance and stature are positively correlated with precipitation (Taub, 2000; Bocksberger et al., 2016). The short-grass/tall-grass boundary occurs at ~750 mm mean annual precipitation (MAP) for the Sudanian, Sahelian, and Somali-Masai phytogeographic zones of western, central, and eastern Africa (van Wyk, 1979; McNaughton, 1983).

Vegetation structure and ecosystem services are vastly different in short- and tall-grass savannas. Short-grass savanna grasses are typically one to several decimeters in height, highly nutritious, heavily grazed, and often form rhizomatous lawns (McNaughton, 1985; Quigley and Anderson, 2014; Hempson et al., 2015b). Short-grass savanna mammals are typified by high species diversity and very high abundances of medium-sized social mixed-diet taxa (e.g., gazelle, oryx, common eland) (Hempson et al., 2015a). Tall-grass savanna grasses can reach heights of one to two meters, are less nutritious (low in N, P, and Na), less palatable/digestible (high lignin and silica), hide predators, and promote high fire frequency and intensity (Dobson, 2009; Pays et al., 2012; Quigley and Anderson, 2014). Tall-grass savanna mammals are typified by high relative abundances of non-ruminant grazers such as equids, hippos, rhinos and suids, and water-dependent grazers such as wildebeest, hartebeest, Hippotragus sp. and Kobus sp. (Hempson et al., 2015a). Hominin behavior may have been very different within these two structurally and compositionally different savanna types. Thus, a major goal of this study is to identify periods of short- and tall-grass dominance and how these two habitat types vary over time.

2.4. Regional and local setting for the drill-core site

The Baringo-Bogoria Basin is part of the eastern branch of the East African Rift System (EARS), and contains present-day Lake Baringo and Lake Bogoria to the south. Like most of the EARS, the Baringo-Bogoria Basin is surrounded by a landscape that is topographically complex, resulting in a high level of plant diversity (Fig. 1). It is likely this complex mosaic of vegetation was in place to some degree in the central Rift Valley by the Pliocene (Jacobs, 2004; Jacobs et al., 2010). A review of the plant fossil record suggests that vegetation complexity has been increasing over the Neogene (Linder, 2017).

The modern 6569 km² Lake Baringo watershed spans an elevation range of ~1000 to > 2000 msl, and encompasses 10 vegetation types that range from open grassland to afromontane forest (van Breugel et al., 2015). The BTB13 drill site is located ~12 km west of Lake Baringo in the Tugen Hills at 1158 msl (Cohen et al., 2016). Modern vegetation at the drill site is classified as Somalia-Masai *Acacia-Commiphora* deciduous bushland and thicket with 40% or more woody cover (White, 1983; van Breugel et al., 2015). The area experiences low and erratic MAP, which varies between 500 and 750 mm, and has annual evaporation rates between 2000 and 2800 mm (Ngaira, 2005). Little is known about the extent and depth of the Chemeron Formation paleolakes, but the depocenter may have been to the east of the drill site (Deino et al., 2006).

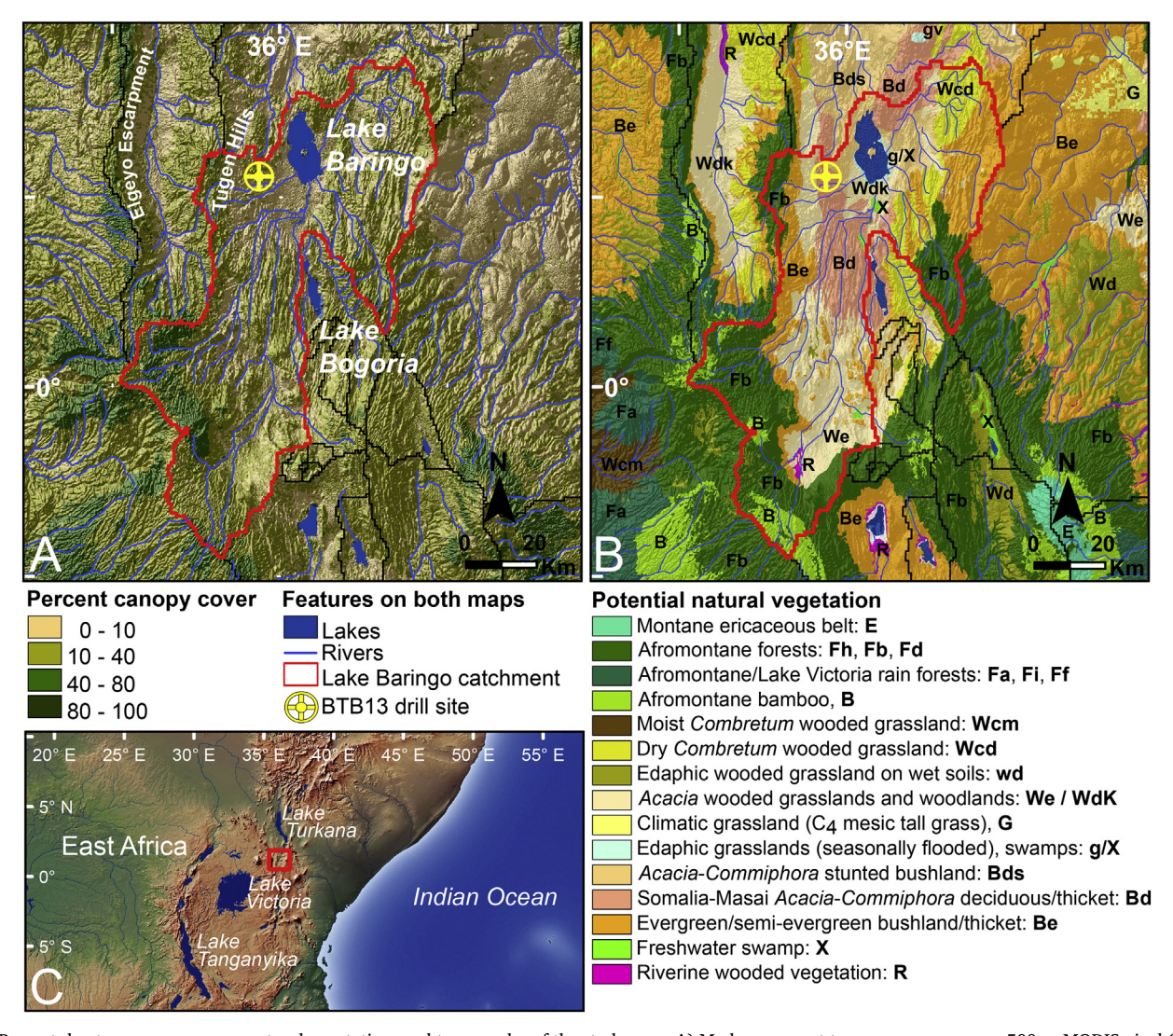


Fig. 1. Present-day tree-canopy cover, natural vegetation, and topography of the study area. A) Modern percent tree canopy cover per 500-m MODIS pixel (Hansen et al., 2003) with cover classes used by White (1983) for African vegetation type (formation) descriptions. B) Potential natural vegetation from van Breugel et al. (2015), which is based on White's original vegetation map of Africa, but mapped at higher resolution. C) Shaded relief map of eastern Africa showing the Baringo Basin (red box). (For interpretation of the references to colour in this figure legend, the reader is referred to the web version of this article.)

3. Methods

3.1. Drill core extraction and core chronology

A single, vertical 227.9 m borehole was drilled at the Tugen Hills site (Lat 0°33′16.56" N, Long 35°56′15.00" E) in May–June 2013. BTB13 was drilled using truck-mounted standard wireline diamond bit drilling with standard IODP butyrate core liners. The 228 m of core was airfreighted to LacCore, the National Lacustrine Core Facility (University of Minnesota, USA) for full scanning, processing, description, and subsampling. See Cohen et al. (2016) for coring details and initial core descriptions. Core depths are reported in meters below surface (mbs). A Bayesian stratigraphic age model for the core was developed by Deino et al. (2020) using 40 Ar/ 39 Ar dating, magnetostratigraphy, and tephrostratigraphy.

3.2. Microfossil separations from sediment

With the exception of core intervals with voids, approximately 2 cm³ of sediment was initially collected for pollen and phytolith/microcharcoal separations every 32 cm along the 228 m core, resulting in 652 samples. Pollen and phytolith/microcharcoal samples were split at

the University of Arizona, and ages for each sample were assigned from the age model. On average, each sample encompasses 66 years, with 1093 years between samples.

3.2.1. Phytolith, pollen, and microcharcoal separations

Phytoliths and microcharcoal particles were extracted together and counted on the same slide. All 652 samples were analyzed for phytoliths and microcharcoal using a modified version of the wet-oxidation and heavy-liquid density separation method described in Piperno (2006). In a controlled comparison of microcharcoal separation methods, density separation using a heavy liquid and chemical removal of organic matter produced a significantly higher microcharcoal yield than other common methods (Turner et al., 2008). Additionally, a direct comparison of standard sieve- versus pollen-extracted charcoal (which would agitate charcoal similarly as a phytolith extraction) found that pollen-slide concentrations were higher, but the broad-scale trends in fire between the two approaches were comparable (Carcaillet et al., 2001). Synthetic microspheres were added to each sample in order to calculate concentrations. Detailed extraction steps are provided in the Supplementary Online Material (SOM).

As an initial assessment of pollen preservation, pollen was analyzed at 96 cm intervals (every third sample collected; 108 total). Preliminary

Table 1 Phytolith morphotypes used for analysis, interpretation, and index calculations.

$\frac{1}{10000000000000000000000000000000000$	
Rondel-angular keel Leaf/Culm/Inflor. Yost et al., 2018 Phalaris spp. C ₃ grass Ic ₃ , D/P	
Rondel-keeled Leaf/Culm/Inflor. Fredlund and Tieszen, 1994 Pooideae C ₃ grass Ic ₃ , D/P	
Rondel-length > 15 µm Leaf/Culm/Inflor. Barboni and Bremond, 2009 Pooideae C ₃ grass Ic ₃ , D/P	
Trapeziform sinuate & Trapezoid Leaf/Culm/Inflor. Madella et al., 2005 Pooideae C ₃ grass Ic ₃ , D/P	
Plateaued saddle Leaf/Culm/Inflor. Piperno and Pearsall, 1998; Yost et al., 2018 Phragmites spp. C ₃ grass Ic ₃ , D/P	
Very tall saddle (VTS) Leaf/Culm/Inflor. Piperno and Pearsall, 1998; Yost et al., 2018 Bambusoideae C ₃ grass Ic ₃ , D/P	
Rondel/Bilobate-irregular Leaf/Culm/Inflor. Piperno and Pearsall, 1998 Bambusoideae C_3 grass Ic_3 , D/P	
Bilobate angulate–asym. lobes $Leaf/Culm/Inflor$. Esteban et al., 2017 Danthonioideae C_3 grass Ic_3 , D/P	
Bilobate–scooped ends Leaf/Culm/Inflor. Yost and Blinnikov, 2011; Neumann et al., Ehrhartoideae C ₃ grass Ic ₃ , D/P 2017	•
Saddle Leaf/Culm/Inflor. Madella et al., 2005 Chloridoideae C ₄ xeric grass Ic ₃ , D/P	°, Iph
Rondel-spool/horned Leaf/Culm/Inflor. Lu and Liu, 2003 cf. Chloridoideae C ₄ xeric grass Ic ₃ , D/P	•
Bilobate: B/VLL/VLS Leaf/Culm/Inflor. Neumann et al., 2017 cf. Aristidoideae C ₄ xeric grass Ic ₃ , D/P	°, Iph
Cross: Triangle Leaf/Culm/Inflor. Neumann et al., 2017 Panicoideae C ₄ mesic grass Ic ₃ , D/P	°, Iph
Cross: Q/VLL Leaf/Culm/Inflor. Neumann et al., 2017 Panicoideae C ₄ mesic grass Ic ₃ , D/P	°, Iph
Cross: Q/LL Leaf/Culm/Inflor. Neumann et al., 2017 Panicoideae C ₄ mesic grass Ic ₃ , D/P	°, Iph
Cross: Q/ML Leaf/Culm/Inflor. Neumann et al., 2017 Panicoideae C ₄ mesic grass Ic ₃ , D/P	°, Iph
Cross: Q/SL Leaf/Culm/Inflor. Neumann et al., 2017 Panicoideae C ₄ mesic grass Ic ₃ , D/P	-
Bilobate: B/VLL/LS Leaf/Culm/Inflor. Neumann et al., 2017 Panicoideae C ₄ mesic grass Ic ₃ , D/P	-
Bilobate: B/LL/VLS Leaf/Culm/Inflor. Neumann et al., 2017 Panicoideae C ₄ mesic grass I _{C3} , D/P	
Bilobate: B/LL/LS Leaf/Culm/Inflor. Neumann et al., 2017 Panicoideae C ₄ mesic grass I _{C3} , D/P	
Bilobate: B/LL/SS Leaf/Culm/Inflor. Neumann et al., 2017 Panicoideae C ₄ mesic grass Ic ₃ , D/P	
Bilobate: B/LL/Con Leaf/Culm/Inflor. Neumann et al., 2017 Panicoideae C ₄ mesic grass Ic ₃ D/P	-
Bilobate: B/ML/LS Leaf/Culm/Inflor. Neumann et al., 2017 Panicoideae C ₄ mesic grass Ic ₃ , D/P	-
Bilobate: B/ML/SS Leaf/Culm/Inflor. Neumann et al., 2017 Panicoideae C4 mesic grass Ic3, D/P	-
Bilobate: B/ML/Con Leaf/Culm/Inflor. Neumann et al., 2017 Panicoideae C4 mesic grass Ic3, D/P	-
	-
, , , , , , , , , , , , , , , , , , , ,	-
Polylobate Leaf/Culm/Inflor. Neumann et al., 2017 Panicoideae C ₄ mesic grass Ic ₃ , D/P	, ipii
Multicellular long cell fragment Leaf/Culm/Inflor. Rosen, 1992 Poaceae Grass ^b	
Bulliform-cuneiform/rectangular Leaf Madella et al., 2005 Poaceae Grass ^{b, c}	
Trichome (Poaceae-type) Leaf/Culm/Inflor. Madella et al., 2005 Poaceae Grass ^b	
Substomatal/stomatal complex Leaf Yost et al., 2018 Poaceae Grass ^b	
Dendritic long cell Inflorescence Madella et al., 2005 Poaceae Grass	
Elongate psilate long cell Leaf/Culm/Inflor. Madella et al., 2005; Yost et al., 2018 Poaceae & Cyperaceae Grass/Sedge ^b	
Elongate echinate long cell Leaf/Culm/Inflor. Madella et al., 2005; Yost et al., 2018 Poaceae & Cyperaceae Grass/Sedge Grass/Sedge	
Blocky w/dark infilling Leaf/Culm Novello et al., 2012 Poaceae & Cyperaceae Grass/Sedge ^b	
Thin sheets w/ridges (TWR) Culm Yost et al., 2018 Cyperaceae Sedge	
Irreg. w/tubular projections Root/Rhizome Yost et al., 2018 Cyperaceae Sedge	
Cone cell–psilate/rounded Leaf/Culm/Inflor. Ollendorf, 1992 Cyperaceae Sedge	
Cone cell–verrucate/polyhedral Achene (seed) Ollendorf, 1992; Piperno, 2006 cf. Cyperus/Kyllinga Sedge	
Perforate decorated Leaf da Costa et al., 2018 Tristicha trifaria Aquatic	
Prismatic domed cylinder Seed Eichhorn et al., 2010; Yost ref. collection Commelina spp. Herbaceous	
Conical truncated Seed Eichhorn et al., 2010 cf. Murdannia /Floscopa Herbaceous	
Pyramidal w/ridges Leaf Levin, 2019 cf. Cyclosorus spp. Herbaceous	
Conical echinate Leaf Benvenuto et al., 2015; Prychid et al., 2003 Orchidaceae Herbaceous	
Elongate irregular Bark Collura and Neumann, 2017 Tree/Shrub	
Elongate facetate Bark Collura and Neumann, 2017 Tree/Shrub	
Sclereid pitted ^d Bark Collura and Neumann, 2017 Tree/Shrub	
Irregular striate/verrucate ^d Leaf/Wood Wallis, 2003; Scurfield et al., 1974 Tree/Shrub	
Blocky facetate Bark Collura and Neumann, 2017 Tree/Shrub	
Blocky irregular Bark Collura and Neumann, 2017 Tree/Shrub	
Blocky w/irreg. proj. Bark Collura and Neumann, 2017 Bignoniaceae Tree/Shrub	
Globular granulate Bark/Wood Collura and Neumann, 2017 Discussed in text Tree/Shrub D/P°	
Globular psilate Bark/Wood Collura and Neumann, 2017 Tree/Shrub	
Ellipsoid echinate Bark Collura and Neumann, 2017 cf. Boscia Tree/Shrub	
Nodular Mostly Wood Collura and Neumann, 2017 Discussed in text Tree/Shrub	
Granular Wood Collura and Neumann, 2017 Discussed in text Tree/Shrub	
Blocky cavate Bark Collura and Neumann, 2017 cf. Celtis Tree/Shrub Clabular achinate Rank Leaf Represents at al. 2015; Albert et al. 2009 Argenceae (palms) Tree/Shrub	
Globular echinate Bark, Leaf Benvenuto et al., 2015; Albert et al., 2009 Arecaceae (palms) Tree/Shrub Footback blocky (clabular Leaf Veelbefor and Pinerro 1008; Pinerro 2006 Apparences Tree/Shrub	
Facetate blocky/globular Leaf Kealhofer and Piperno, 1998; Piperno, 2006 Annonaceae Tree/Shrub Anticlinal enidermic sheet Leaf Richard Piperno, 2006 Annonaceae Tree/Shrub	
Anticlinal epidermis sheet Leaf Piperno, 2006 Tree/Shrub	

^a Because of issues with taxonomic multiplicity and redundancy, there are few to no phytolith morphotypes unequivocally diagnostic of grass subfamilies or plant functional types (PFTs). However, the dominant association of particular morphotypes with grass subfamily membership, photosynthetic pathway, and/or ecological requirements allows for the generalized taxonomic and PFT interpretations used here.

b These morphotypes were lumped into a category called 'drought-stressed and wetland graminoids', based in part on Issaharou-Matchi et al. (2016).

^c We attempt to separate Poaceae bulliform cells from similar Cyperaceae cells by use of the morphotype 'Blocky w/dark infilling'.

^d These two morphotypes were lumped together during counting but in retrospect should have been separated.

results suggested that pollen concentrations in the BTB13 samples were very low, necessitating larger than normal sample volumes. For all 108 samples, $\sim\!\!10$ g of sediment was processed using standard methods of Faegri and Iversen (1989) and sieved at 10 $\mu m.$ Lycopodium tablets were added to each sample in order to verify pollen preservation and to calculate concentrations.

3.3. Microscopy: phytolith, pollen, and microcharcoal identifications

3.3.1. Phytoliths and microcharcoal

Entire samples or subsamples were mounted on microscope slides using Permount and sealed with fingernail polish just prior to counting. Permount requires several days to dry completely, allowing in the meantime for phytolith rotation, which is essential for many phytolith identifications. Phytolith and microcharcoal counting was conducted using an Olympus BX-43 transmitted-light microscope at $400 \times \text{magnification}$, with a goal of 200 index-specific phytoliths counted (Strömberg, 2009).

The phytolith classification used 60 phytolith morphotypes. The primary descriptive reference(s), anatomical origin, and taxonomical interpretation for each morphotype are listed in Table 1. Morphotype names used were either derived from the International Code for Phytolith Nomenclature (ICPN 1.0; Madella et al., 2005) or from the primary references used to identify them. This classification includes the use of the bilobate and cross supertypes suggested by Neumann et al. (2017). Microcharcoal was identified (absolute counts) using the diagnostic characteristics described by Turner et al. (2008), with particular emphasis on avoiding misidentifications from pyrite and unburned plant fragments that may have darkened naturally over time.

3.3.2. Pollen

Pollen residues were mounted onto slides in glycerol and sealed with fingernail polish. Because of low pollen yields, two slides were made for each sample and completely scanned using transmitted-light microscopy at 400 × magnification to verify the presence of identifiable pollen, algae, and other non-pollen palynomorphs. Samples with no pollen present were marked as "sterile", and no further analysis was conducted. For samples with at least one identifiable pollen grain, five further slides were mounted, and pollen was identified using atlases of pollen morphology and the African Pollen Database (e.g., Maley, 1970; Bonnefille and Riollet, 1980). No samples yielded more than 12 pollen grains. Low pollen concentrations require that the data presented here be considered qualitative and not completely or robustly representative of the ancient flora, and that the absence of a pollen type does not necessarily indicate its absence on the landscape. The pollen analysis resulted in the identification of 14 pollen taxa plus fern spores and green algae. The nomenclature for these follows Vincens et al. (2007).

3.4. Phytolith abundance and index calculations

Percent relative-abundance calculations were based on the total phytolith count for each sample. Concentrations were calculated from the microsphere counts and starting volume of the sample (SOM Table S1). Influx values reported as particles per cm² per year were based on calculated concentrations and sedimentation rates determined from the age model. The relative abundance plot of C3, C4 mesic, and C4 xeric grass phytoliths was based solely on grass silica short-cell (GSSC) phytoliths attributed to those plant functional types (Table 1). The tree cover (D/P°) and aridity (Iph) phytolith indices were calculated as described in Bremond et al. (2008) and Yost et al. (2018) using the specific morphotypes listed in Table 1. The 95% confidence intervals (CI) for the D/P° and Iph indices were determined by nonparametric bootstrap resampling using the 'boot' and 'simpleboot' packages in R (R Core Team, 2018). The R bootstrapping and error propagation code written to run on lists of D/P° and Iph values is provided in the SOM. The Ic₃ index used here is a variant of the Ic climatic index described in Bremond et al. (2008). We calculate the Ic_3 index by including all GSSC morphotypes ascribed as being derived from a C_3 or C_4 grass in Table 1, which then becomes $(C_3 / C_3 + C_4) \times 100$.

3.5. Statistical and time series analyses

Detrended canonical correspondence analysis (DCCA) was conducted on the counts of specific phytolith morphotypes using CANOCO ver. 4.55 (ter Braak, 1986). Only the morphotypes ascribed to a particular taxonomic level (Table 1) were included in the analysis. Grass morphotypes that could not be identified lower than family level (Poaceae) were not included. All cross and bilobate types were summed into one category (Panicoideae), as were all woody dicot morphotypes (trees), excluding palms. DCCA applied to stratigraphic plant data with age as the only constraint (temporal gradient) yields an estimate of adjacent sample plant taxa compositional turnover in units of standard deviation (Birks, 2007).

Time series (spectral) analysis was conducted using PAST ver. 3.2 (Hammer et al., 2001). Lomb periodograms were produced using the REDFIT procedure with a rectangular window function, and confidence intervals were determined using 1000 Monte Carlo simulations (Schulz and Mudelsee, 2002). Spectral analysis was applied to the entire microcharcoal concentration record, and to $\rm D/P^{\circ}$ and Iph index values from three intervals with good preservation. The microcharcoal concentration data was log transformed (because of non-Gaussian high amplitude variability), detrended, and linearly interpolated to 1200 yr time steps prior to analysis. The $\rm D/P^{\circ}$ and Iph data were detrended and linearly interpolated to 1500 and 1100 yr time steps, respectively, prior to analysis.

3.6. Compilation of relevant modern phytolith assemblages from Africa

A total of 168 samples (SOM Table S2) were selected from 10 published modern phytolith datasets compiled from eastern and western Africa (Alexandre et al., 1997; Barboni et al., 1999; Runge, 1999; Bremond et al., 2005a; Bremond et al., 2005b; Bremond et al., 2008; Garnier et al., 2012; Novello et al., 2012; Arráiz et al., 2017; Barboni et al., 2019) to assess the relationship between D/P° values and tree cover, and the relative abundances of palm (Arecaceae), woody dicotyledonous (trees), and GSSC (grass; Poaceae) phytoliths (A:D:P) with vegetation formation in the form of a ternary plot. To accomplish this, each modern D/P° and A:D:P sample was assigned to a basic vegetation formation type and woody canopy cover based on White (1983) as follows: swamp (open), shrubland (open), bushland (> 40% short woody cover) grassland (0–10% tree cover), wooded grassland (10–40% tree cover), woodland (40–80% tree cover), forest (80–100% tree cover).

4. Results

4.1. Phytolith and microcharcoal recovery

Phytolith preservation and recovery in BTB13 varied from excellent to poor, with some intervals yielding no phytoliths, ostensibly the result of total dissolution of biogenic silica (Figs. 2 and 3; Table 2). When progressing from older to younger sediments (core bottom to top), a repeated dissolution succession was observed over 19 times. As sediment pore water salinity and pH increased, as inferred by increasing fragmentation and depth and width of dissolution pits, diatoms and sedge cone cell phytoliths were the first microfossils to disappear, followed by small phytoliths (e.g., GSSCs), then, elongate, trichome, and bulliform phytoliths, followed by sponge spicules. Finally, sponge spherasters were the last microfossils observed in the dissolution succession. Diatom, phytolith, and sponge microfossils would often reappear in the opposite order as pH apparently trended towards neutral values.

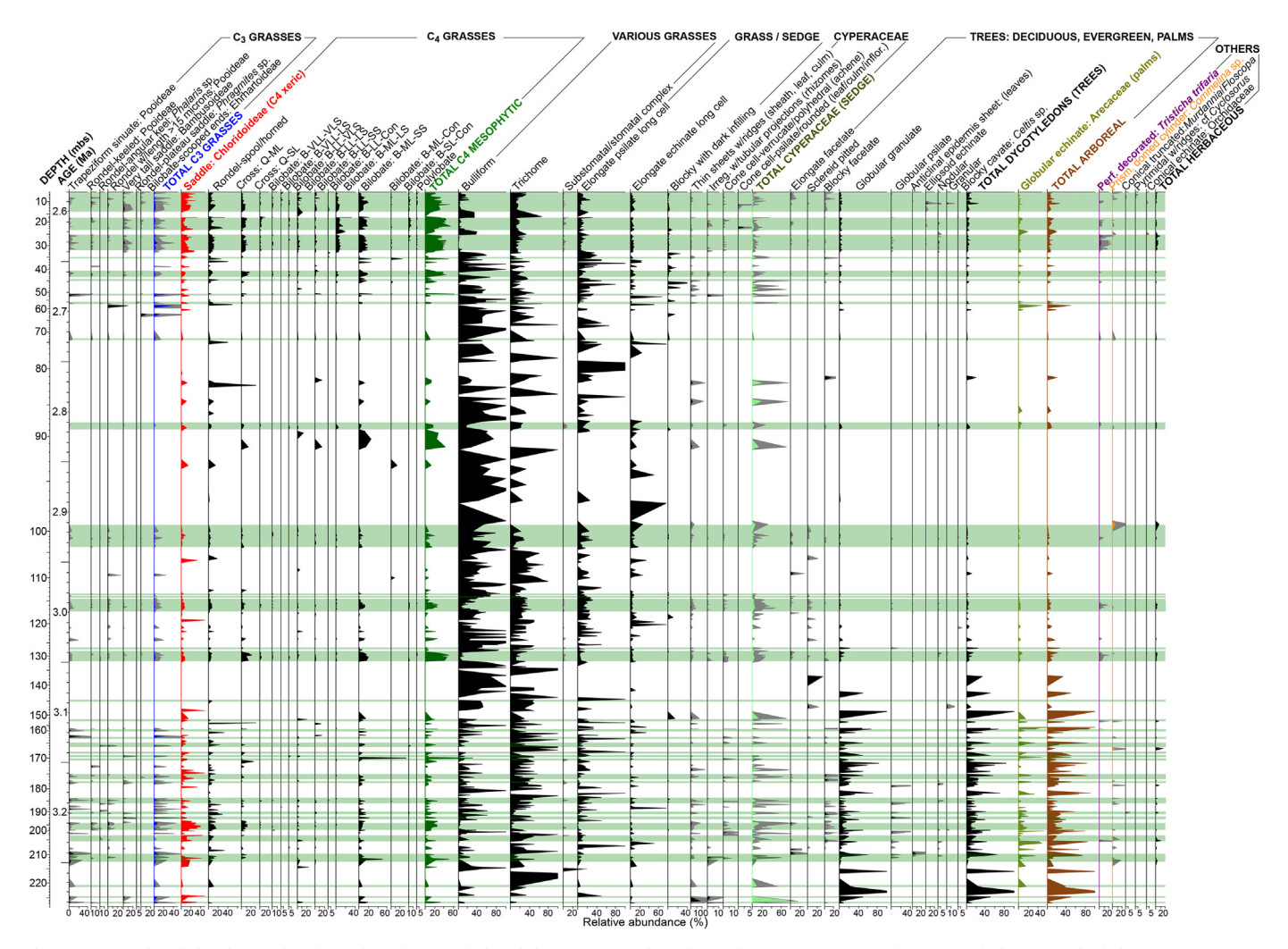


Fig. 2. BTB13 phytolith relative abundance based on total phytolith counts for selected morphotypes. Some morphotypes include a gray shaded $5 \times$ exaggeration. Green shaded zones are intervals with good phytolith preservation. Unshaded (white) intervals had poor phytolith preservation, which precluded unbiased calculations of the Iph and D/P° indices. (For interpretation of the references to colour in this figure legend, the reader is referred to the web version of this article.)

Intervals with either generally good or poor phytolith preservation delineated the five zones identified in Fig. 3. Of the 652 phytolith samples analyzed, 161 (25%) yielded no phytoliths. Additionally, 311 samples (48%) did yield few to many phytoliths, but low to no GSSC phytolith recovery precluded the calculation of D/P°, Ic3, and Iph indices, and A:D:P on those samples. However, 180 samples (27%) scattered throughout the core yielded well-preserved phytoliths with no evidence of morphotype assemblage bias. Because of significant differences in phytolith preservation and vegetation composition, the following sections often highlight pre- and post-3.04 Ma values.

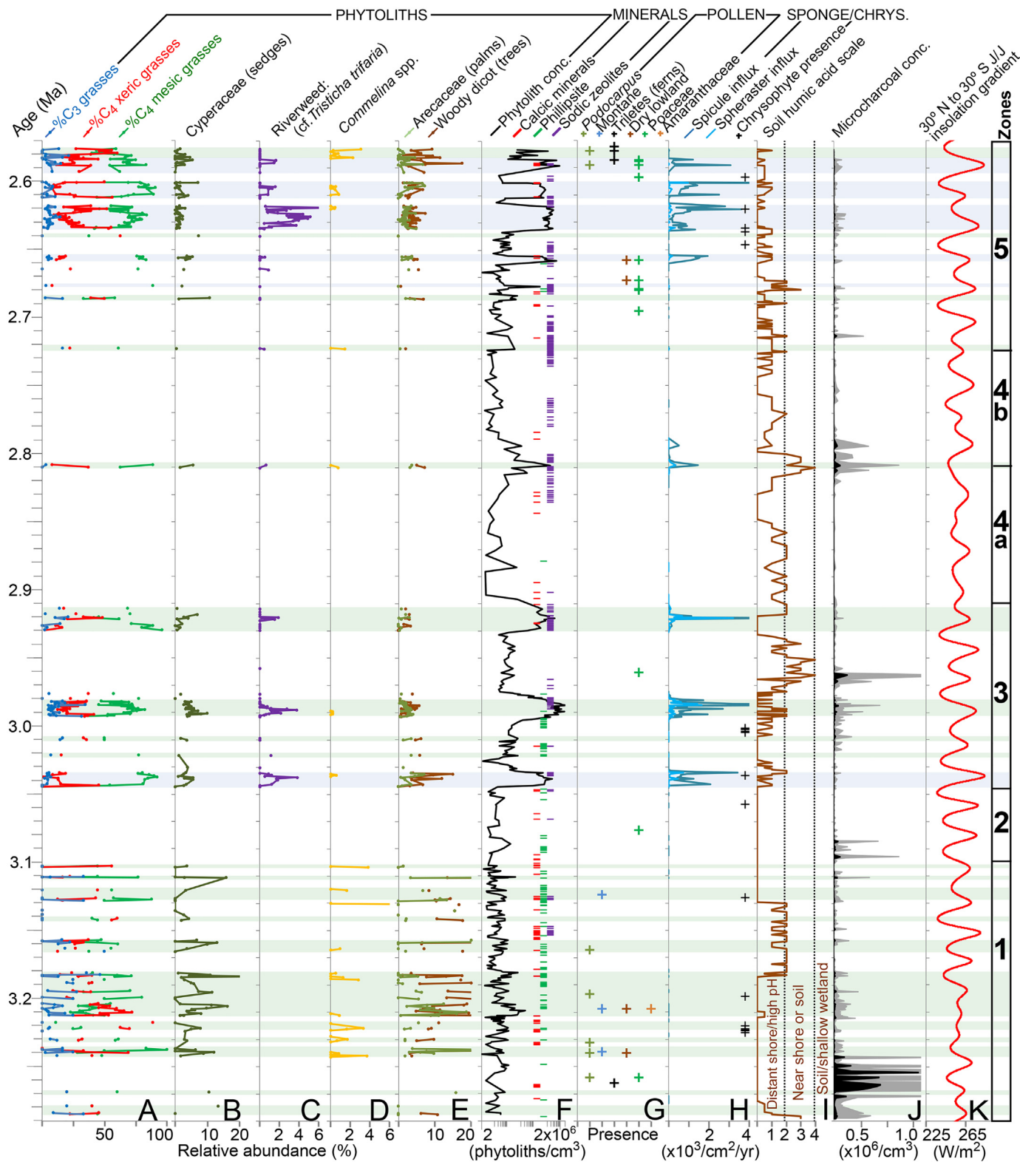
A total of 50,520 phytoliths were counted from BTB13 material, with the number per sample ranging from 0 to 1866. Phytolith concentrations by volume varied between 0 and 6.728 \times 10^6 per cm³ (Fig. 3F). Phytolith influx varied between 0 and 1.2×10^5 per cm² yr $^{-1}$ (SOM Table S1). Average phytolith concentration and influx before 3.04 Ma was 93 per cm³ and 6.8 per cm² yr $^{-1}$, and after 3.04 Ma was 1.39×10^5 per cm³ and 3736 per cm² yr $^{-1}$, respectively. Low phytolith concentration values early in the record for the well-preserved samples were associated with coarse-grained alluvial and fluvial sediments (Scott et al., 2020). Good phytolith preservation before 3.04 Ma typically coincided with insolation minima and extended periods of dampened insolation maxima. High-amplitude peaks in phytolith concentrations and well-preserved intervals after 3.04 Ma are typically coincident with insolation maxima.

Microcharcoal was recovered in all samples. Microcharcoal

concentrations varied between 30 and 1.556×10^6 per cm³ (Fig. 3*J*) and influx varied between 1 and 7.6×10^4 per cm² yr¹ (SOM Table S1). Average microcharcoal concentrations before and after 3.04 Ma were 35,732 and 6487 per cm³, decreasing by a factor of 5 after 3.04 Ma. Influx values decreased 10-fold after 3.04 Ma. Phytoliths darkened from exposure to fire were rare and their occurrence was not included in the analysis.

Phytoliths from woody dicots (trees), Arecaceae (palms), Cyperaceae (sedges), C_3 Pooideae grasses, and dayflower (*Commelina* spp.) (Figs. 3 and 4) are most abundant from the bottom of the core at \sim 3.29 Ma to 3.04 Ma. Phytoliths diagnostic of riverweed (*Tristicha trifaria*, Podostemaceae), an aquatic plant that only grows on rocks in rapids and waterfalls at low and high elevations (Agnew, 2013; Koi et al., 2015), appears in the record only after 3.04 Ma. Peaks in riverweed abundance are coincident with insolation maxima. Phytoliths from bamboo (Bambusoideae) and orchids (Orchidaceae), which are typically montane vegetation indicators (Agnew, 2013), are most abundant after 2.59 Ma. Possible fern phytoliths (cf. *Cyclosorus* sp.) and *Murdannia/Floscopa*-type phytoliths, indicators of freshwater swamps (Lind and Morrison, 1974), are almost exclusively observed after 2.59 Ma.

When just comparing the relative abundances of C_3 , C_4 mesic, and C_4 xeric GSSC phytoliths, average C_4 xeric grass values before and after 3.04 Ma are 38% and 25%. For C_3 grasses, the before and after 3.04 Ma averages are 12% (max 50%) and 8% (max 35%), respectively.



(caption on next page)

Paradoxically, arid-adapted C_4 grasses and mesic/cool/shade-adapted C_3 grasses were both more abundant before 3.04 Ma. This insolation-phytolith preservation relationship is discussed in detail in Section 6.1.1.

4.2. Other siliceous microfossils recovered

Diatoms, chrysophyte stomatocysts, sponge spicules, and sponge spherasters were also recovered with the phytolith extracts (Figs. 2, 3*H*, and 5). Because BTB13 diatoms were studied in detail by Westover et al. (2020), only diatom presence and absence was recorded. Freshwater siliceous sponge spicules and spherasters were counted, and at times

Fig. 3. Summarized phytolith, pollen, microcharcoal, sponge, chrysophyte cyst, and mineralogy datasets from BTB13. Horizontal blue bars delineate periods with high diatom concentrations and good phytolith preservation. Horizontal green bars delineate periods with few or no diatoms, but with good phytolith preservation. Regions with no phytolith data suffer from complete biogenic silica dissolution or exhibit preservation biases that prohibit relative abundance or index calculations. Zones (right axis) represent intervals with either generally good (odd numbered) or poor (even numbered) phytolith preservation. A) Relative abundance of grass silica short cell (GSSC) phytoliths ascribed to C_3 and C_4 functional types. B) Percentage of sedge (Cyperaceae) phytoliths. C) Percentage of riverweed (*Tristicha trifaria*, Podostemaceae) phytoliths. D) Percentage of dayflower (*Commelina* spp.) phytoliths. E) Percentage of palm (Arecaceae) and ligneous dicot (tree) phytoliths. F) Phytolith concentrations (log scale per cm³) plotted with mineral presence/absence from XRD analysis. Calcic minerals include calcite, low-Mg calcite, and dolomite. Sodic zeolites include heulandite-clinoptilolite, chabazite, and analcime. G) Pollen presence/absence (most samples were pollen sterile). H) Influx rate of sponge spicules and spherasters (per cm² yr⁻¹), and presence of chrysophyte cysts. I) Relative abundance of soil humic acids based on a colour scale after removal with KOH during the phytolith extraction procedure. J) Microcharcoal concentrations (log scale per cm³) with $10 \times exaggeration$ in gray shading. K) 30° N to 30° S June insolation gradient with parameters calculated using INSOLA (Laskar et al., 2004). (For interpretation of the references to colour in this figure legend, the reader is referred to the web version of this article.)

found to be very abundant. Sponge spicule concentrations varied between 0 and 5.24 \times 10^5 ($\overline{x}=6.4\times10^3$) per cm 3 . Very distinctive sponge asterose microscleres (Fig. 5.7), consistent with those produced by the freshwater sponge *Dosilia brouni* (Manconi and Pronzato, 2009), were observed at 131.58 mbs (3.04 Ma) and 160.77 mbs (3.12 Ma), along with *Dosilia*-like microscleres and gemmuloscleres. Concentration values for sponge spherasters, which have a striking similarity to palm (Arecaceae) phytoliths, varied between 0 and 1.13 \times 10^5 per cm 3 ($\overline{x}=1.3\times10^3$).

4.3. Pollen recovery

Pollen recovery was poor throughout the record. Of the 108 samples processed for this study, 80 yielded no identifiable pollen and were considered sterile. The remaining 28 samples contained at least one grain of identified pollen (Fig. 3*G*; Table 2), however, all concentrations

were extremely low (the highest concentration was < 1 grain per g dry sediment). Subaerial exposure and/or high-oxygen pore waters (oxidation) may have severely degraded the pollen record.

4.4. Compilation of modern D/P° tree cover index values

Boxplots of the selected 168 modern D/P° values are presented in Fig. 6. From lowest to highest, the mean D/P° values are as follows: shrubland, 0.08 (n=27, $\sigma=0.10$); grassland, 0.12 (n=15, $\sigma=0.13$); wooded grassland, 0.21 (n=43, $\sigma=0.27$); swamp, 0.21 (n=10, $\sigma=0.21$); bushland, 0.43 (n=5, $\sigma=0.30$); woodland, 1.31 (n=29, $\sigma=0.40$); and forest, 8.51 (n=39, $\sigma=4.11$).

The D/P° index could not distinguish vegetation types with < 40% tree cover. However, a D/P° value of 1 separates all but three woodland samples with > 40% tree cover, one of which is nearly 2 σ from the mean, and all of which are located near the edge of a present-day

 Table 2

 List of plants identified from BTB13 sediment pollen and phytoliths.

Plant group	Family	Subfamily/Tribe	Genus/Species	Indicator
Dicotyledons (Ligneous trees and shrubs):				Phytoliths
	Amaranthaceae			Pollen
	Annonaceae			Phytoliths
	Bignoniaceae			Phytoliths
	Boraginaceae		Cordia-type	Pollen
	Burseraceae		Commiphora ^a	Pollen
	Capparaceae		Boscia	Phytoliths
	Cannabaceae (Ulmaceae)		Celtis	Phytoliths, poll
	Euphorbiaceae		Macaranga-type	Pollen
	Fabaceae		Cassia ^a	Pollen
			Indigofera ^a	Pollen
	Myricaceae		Myrica ^b	Pollen
	Myrtaceae		Syzygium ^b	Pollen
	Podocarpaceae		Podocarpus ^c	Pollen
	Rhamnaceae		Ziziphus-type ^a	Pollen
	Rosaceae		Prunus africana-type ^b	Pollen
Monocotyledons	Poaceae		, ,,	Pollen
		Panicoideae		Phytoliths
		Arundinoideae	Phragmites	Phytoliths
		Chloridoideae		Phytoliths
		Aristidoideae	Aristida	Phytoliths
		Bambusoideae		Phytoliths
		Ehrhartoideae		Phytoliths
		Pooideae		Phytoliths
		Pooideae	Phalaris	Phytoliths
	Cyperaceae			Phytoliths
	71		Cyperus / Kyllinga-type	Phytoliths
	Arecaceae		31, 3	Phytoliths
	Commelinaceae	Commelineae	Commelina	Phytoliths
			C. diffusa	Phytoliths
			Murdannia / Floscopa-type	Phytoliths
	Orchidaceae			Phytoliths
	Podostemaceae	Tristichoideae	Tristicha trifaria	Phytoliths
Pterophytes	Thelypteridaceae	Thelypteridoideae	cf. Cyclosorus	Phytoliths
	Triletes	- ner, premarada	<i>Gy 0.000.</i> au	Pollen

a Dry lowland indicator.

^b Montane indicator.

^c Afromontane indicator.

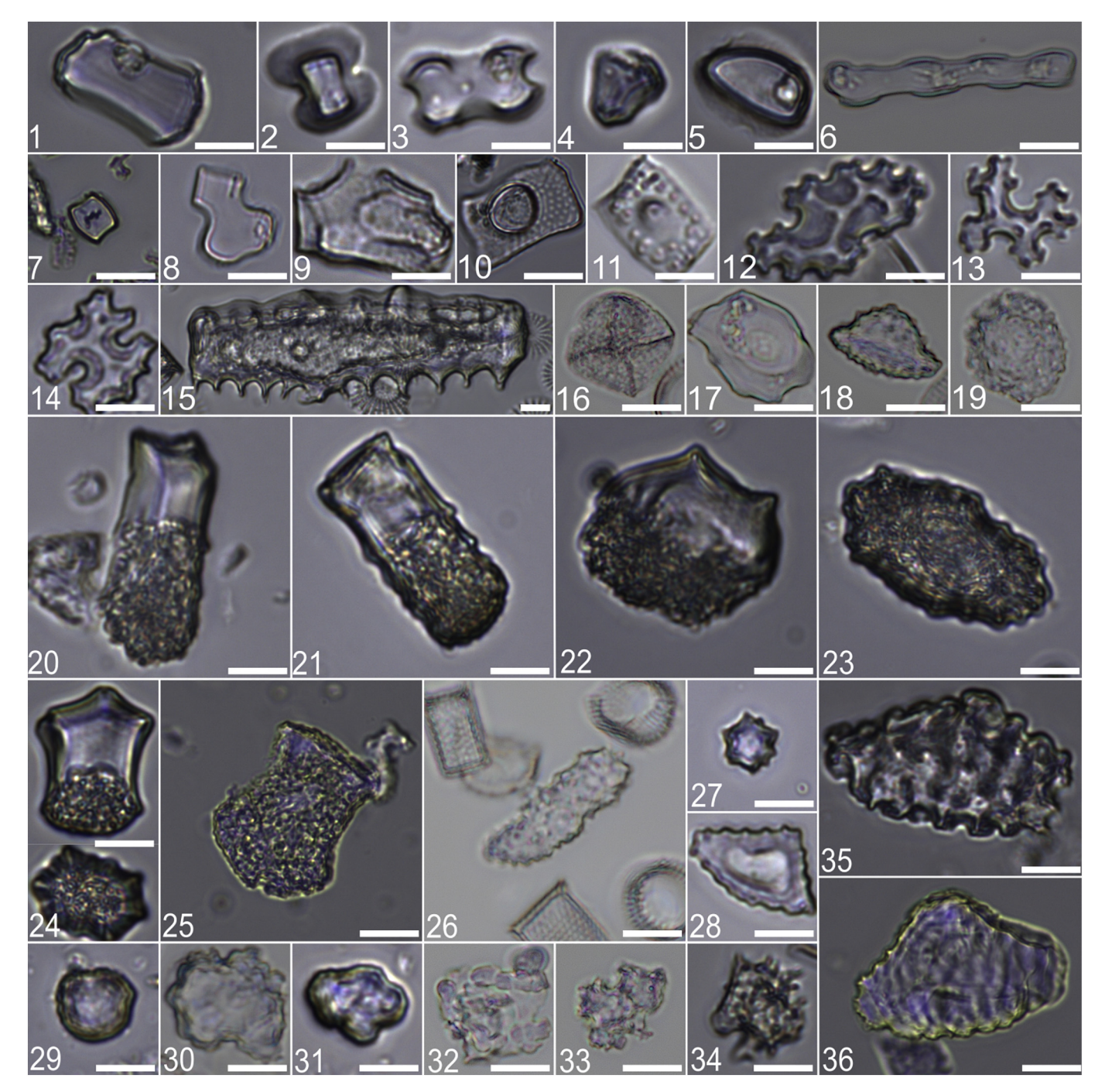


Fig. 4. Selected distinctive and diagnostic phytoliths recovered from the Baringo-Tugen Hills-Barsemoi (BTB13) drill core (white scale bar equals 10 µm). Grasses (Poaceae) 1-8, 15. Sedges (Cyperaceae) 9-11, 15. Herbaceous plants 12-14, 16-25. Trees and shrubs 26-36. (1) Very tall saddle (VTS) considered diagnostic for C₃ Bambusoideae (bamboo) grasses. (2) C₄ Panicoideae bilobate type B/ML/Con after Neumann et al. (2017). (3) C₃ Ehrhartoideae bilobate with scooped ends. (4) Phalaris (C₃ Pooideae) bilobate with angular keel. (5) C₃ Pooideae rondel with length > 15 μm. (6) C₃ Pooideae trapeziform sinuate phytolith. (7) Saddle phytolith typical of C₄ Chloridoideae grasses. (8) Asymmetrical bilobate with one angulate lobe, possibly diagnostic of the C₃ Danthonioideae grass Pentameris (see Esteban et al., 2017). (9) Irregular with tubular projection or circular openings from sedge (Cyperaceae) roots. (10) Sedge (Cyperaceae) achene epidermis cone cell with verrucate surface and polyhedral margins. (11) Sedge (Cyperaceae) leaf/culm epidermis cone cell with satellites surrounding the central papilla. (12-14) Perforate decorated phytoliths diagnostic of C3 emergent aquatic riverweed, Tristicha trifaria (Podostemaceae). (15) Elongate/blocky echinate produced by grasses and sedges. (16) Pyramidal with ridges type possibly diagnostic of the fern Cyclosorus. (17) Conical truncated type typical of C₃ herbaceous plants Murdannia and Floscopa (Commelinaceae). (18–19) Conical echinate type typical of orchids (Orchidaceae) in side (18) and top (19) views. (20–25) Heteropolar (anisopolar) cylinders with a psilate prismatic domed end and a decorated end diagnostic of the C₃ Commelinaceae (see Eichhorn et al., 2010). (20, 21, 24, 25) Commelina africana types representing C. africana, C. bracteosa, C. aspera and C. erecta ssp. erecta). (22-23) Commelina diffusa type in side and top views. (25) Commelina africana type undergoing silica replacement diagenesis. (26) Ellipsoid echinate from bark, possibly diagnostic of Boscia (Capparaceae). (27) Globular echinate diagnostic of palms (Arecaceae). (28) Blocky cavate from bark, possibly diagnostic of Celtis (Cannabaceae). (29-31) Globular decorated morphotypes diagnostic of wood and bark. (32) Nodular morphotype derived typically from the wood of trees. (33-34) Granular morphotype observed in the wood of Rubiaceae and Sapotaceae taxa. (35-36) Irregular morphotypes with verrucate (35) and striate (36) ornamentation observed in tree leaf and woody tissues.

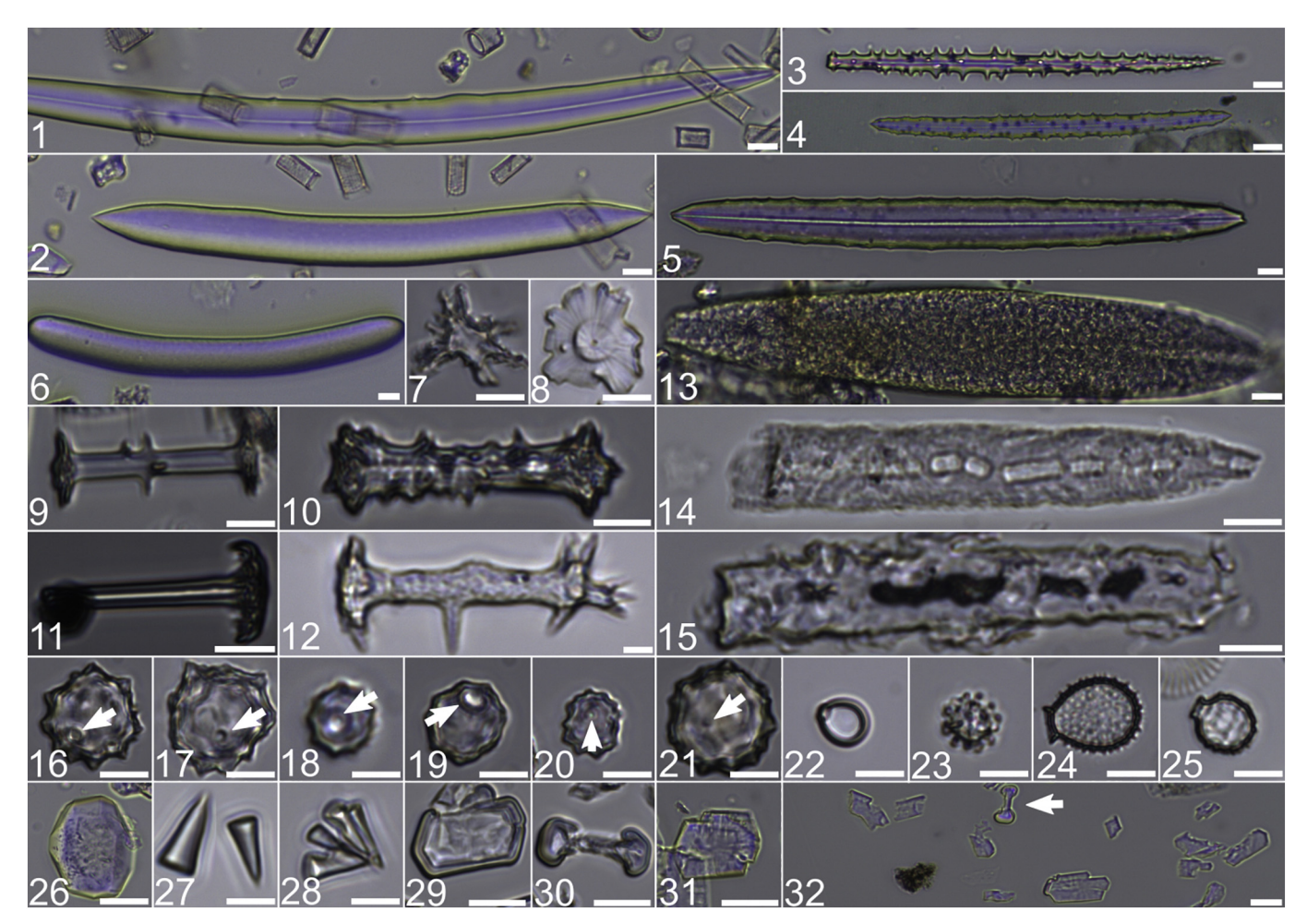


Fig. 5. Selected freshwater sponge and chrysophyte cyst microremains, and non-phytolith evaporites and zeolites recovered from the Baringo-Tugen Hills-Barsemoi (BTB13) drill core (white scale bar equals $10 \mu m$). (1–2) Sponge megasclere oxeas. (3–5) Sponge megasclere acanthoxeas (6) Sponge megasclere strongyle. (7) Sponge asterose microsclere possibly derived from *Dosilia*. (8) sponge gemmulosclere rotule. (9–12) Sponge gemmulosclere birotules, with the birotule in 12 exhibiting minor diagenesis (dissolution). (13–15) Sponge megasclere spicule fragments exhibiting varying types of diagenesis. The spicule in 13 is exhibiting submicron pitting from silica dissolution. The spicules in 14 and 15 are exhibiting devitrification and re-precipitation of silica, with deformation of the axial filament clearly visible. (16–21) Sponge spherasters with arrows pointing to circular openings that range from indistinct to obvious. Spheraster echinate spines become blunted and the circular openings become enlarged as diagenesis progresses. Rotation (3D observation) of globular echinates is essential in separating palm (Arecaceae) phytoliths (see Fig. 4) from sponge spherasters. (22–25) Siliceous stomatocysts from chrysophycean algae. (26) Globular/hemispherical facetate zeolite (cf. analcime). (27–28) Conical zeolites disarticulated in 27 and as a rosette in 28. (29, 31) Thin hexagonal crystalline plates most likely formed as authigenic precipitates or as evaporites. (30, 32) Authigenic precipitate or evaporite resembling a bilobate phytolith morphotype.

woodland patch. The D/P $^{\circ}$ value of 2.2 clearly separates woodland (40–80% tree cover) from forest (> 80% cover), and is similar to the D/P $^{\circ}$ value of 2.0 used by Novello et al. (2017) to distinguish forests from more open savanna habitats. These results are discussed in the SOM.

4.5. Comparison of modern and BTB13 core sample A:D:P

A ternary plot for the percentages of palm (Arecaceae), tree (dicotyledonous/ligneous), and grass short cell (GSSC; Poaceae) phytolith indicators (A:D:P) is plotted in Fig. 7. This plot also includes 180 samples from BTB13. No samples from the core plot within forest or woodland after 3.02 Ma. Among the 17 samples that plot within woodland or forest zones, one plots within semi-evergreen forest, four plot near modern miombo woodlands, two plot near a cluster of modern riparian floodplains, and two plot near palm woodlands. Seven forest samples with 30 to 60% palm phytoliths plot between a palm (swamp) forest sample and a cluster of drier semi-evergreen forest samples. These results suggest most of the BTB13 woodland and forest samples are groundwater-supported vegetation types that may denote swamp, lake margin, or floodplain (riverine) habitats.

4.6. BTB13 core D/P°, Iph, Ic3, and plant turnover indices

4.6.1. D/P° index

The index-specific count size for D/P° ranged from 8 to 233 phytoliths ($\overline{x}=82$). Calculated D/P° values range from 0 to 22, and span open (grassland, wooded grassland, woodland) to closed (forest) vegetation formations (Fig. 8A). However, because of low index-specific count sizes, the bootstrapped 95% CI range varied from 69 to 300% ($\overline{x}=163\%$) of the D/P° value. In many cases, except for those with high D/P° values, the large CIs did not cross a vegetation formation D/P° boundary, and a long-term trend of decreasing woody cover is evident. All but one D/P° value indicating formations of > 40% woody cover occur before 3.10 Ma, and none are observed after 3.02 Ma. Although many of the samples with high D/P° values are from intervals with low phytolith counts, these samples did not exhibit evidence of dissolution.

4.6.2. Iph (short-grass vs. tall-grass) index

The index-specific count size for Iph ranged from 4 to 205 ($\overline{x}=61$). Calculated Iph values ranged from 0 to 89%, spanning the short-grass/tall-grass dominance spectrum (Fig. 8*B*). The bootstrapped 95% CI

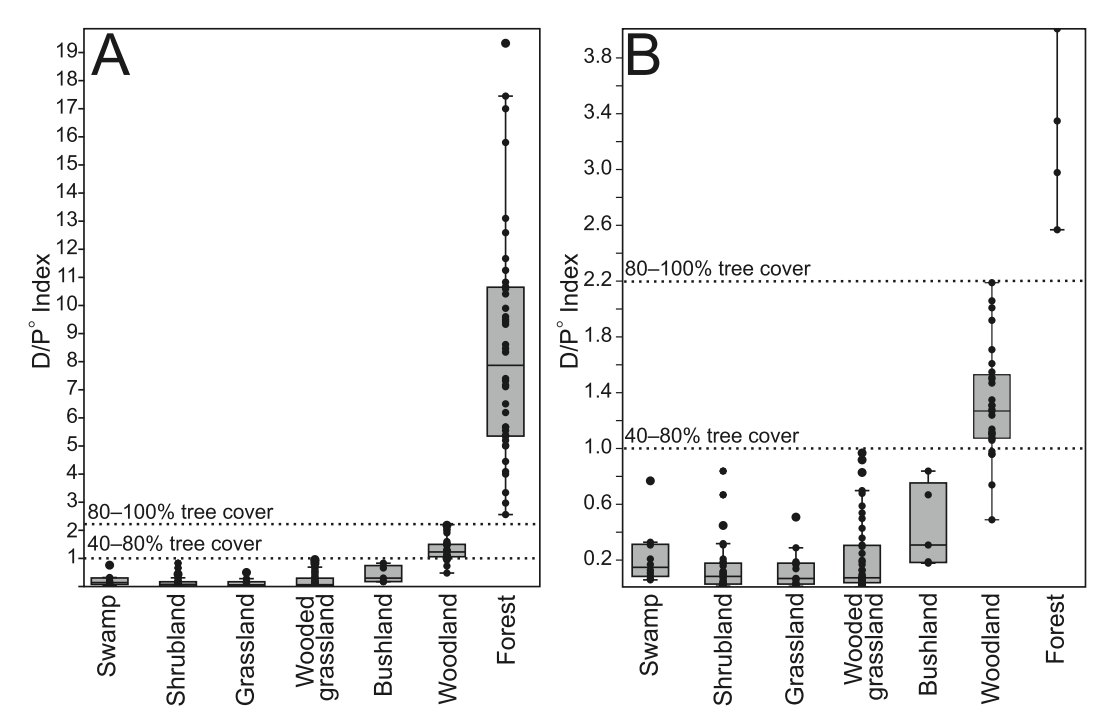


Fig. 6. Boxplots for 168 modern D/P° phytolith index values from western, central, and eastern Africa (SOM Table S2). A) Plots for the entire D/P° range of values. B) Plots for D/P° values between 0 and 4.

range varied from 24 to 300% of the Iph value ($\bar{x} = 102$ %), in agreement with Iph sample size errors identified by Strömberg (2009).

4.6.3. Ic_3 (C_3 grass) index

The index-specific count size for ${\rm Ic_3}$ ranged from 4 to 229 ($\overline{x}=78$). Calculated ${\rm Ic_3}$ values range from 0 to 42% (Fig. 8*C*). Average ${\rm Ic_3}$ values before and after 3.04 Ma are 11% and 6%, respectively. The five highest values ($\overline{x}=34\%$) occur before 2.98 Ma; however, there is no relationship between D/P° and ${\rm Ic_3}$ values ($r^2=0.0008,\ n=123,\ p=.758$), suggesting that ${\rm C_3}$ grass occurrence is neither promoted or suppressed the presence of woody plants.

4.6.4. Plant compositional turnover

The DCCA-derived measure of plant taxa compositional turnover in units of standard deviation is highest during the mid-Piacenzian Warm Period (MPWP, 3.26–3.01 Ma), with adjacent samples varying by an average of 1 σ . After 3.04 Ma the adjacent sample variability was 0.47 σ (Fig. 8D).

4.7. Spectral analysis of Iph and D/P° indices, and microcharcoal concentrations

Results of the REDFIT spectral analyses of D/P° (grass vs. tree cover) and Iph (xeric C_4 short-grass vs. mesic C_4 tall-grass) for three time intervals are provided in Fig. 9. D/P° index variability exhibits precessional periodicity before 2.98 Ma. Iph index variability exhibits precessional periodicity only after 2.98 Ma. Half-precession and quarter-precession periodicities are detected somewhat sporadically between the different indices and time intervals. For the oldest time interval, preservation of contiguous samples spanning the transition from short-grass to tall-grass dominance were limited because phytoliths were mostly preserved only during insolation minima.

Results of the microcharcoal concentration spectral analysis are provided in Fig. 10. There is spectral power well above the 95% confidence level at periodicities of 237, 9.6, and 4.6 kyr (Fig. 10A). Power spectral density of the Lomb periodogram reveals a power dependence on frequency that resembles a 1/f pink noise system (Fig. 10B). The 9.6

and 4.6 kyr periodicities correspond with half precession and quarter precession, respectively. There is no precessional (23–19 kyr) periodicity detected, but precession is likely the carrier of the half-precession signal that arises from the double-peak in charcoal concentrations often associated with peaks in insolation (Fig. 10B). Peaks in mesic C₄ tall-grass abundance vary at precessional periodicity (Fig. 9) and are correlated with peaks in insolation (Fig. 10C).

5. Discussion

5.1. Biogenic silica diagenesis in BTB13

5.1.1. Biogenic silica dissolution succession

To our knowledge, the biogenic silica (BSi) dissolution succession presented in Section 4.1 and illustrated in Fig. 11 has never been previously described for lake sediments. High salinity and pH in sediment pore water are the ostensible cause of poor BSi preservation. These conditions are inferred from the presence/absence of authigenic calcite and zeolites in the XRD analysis of the core (Minkara et al., 2020), many of which commonly form in saline waters at pH \geq 8.5 (Renaut, 1993; Renaut et al., 2002). Zeolites were sometimes in the phytolith extracts themselves, especially when BSi fossils were completely absent (Fig. 3F). Additionally, sponge spherasters, the last BSi microfossils observed in a dissolution succession, sometimes co-occurred with analcime or phillipsite, which typically form in waters with pH ≥ 9.0 (Mariner and Surdam, 1970; Hay, 1986). This reflects the fact that phillipsite, clinoptilolite-heulandite, chabazite, and analcime, the most common zeolites detected in BTB13, have specific gravities that overlap with BSi microfossils.

This BSi dissolution/preservation sequence is not surprising given that differences in size, reactive surface area, and density between diatoms, phytoliths, and freshwater sponges lead to varying dissolution rates under conditions of increasing salinity and pH (Iler, 1979; Bartoli and Wilding, 1980; Barker et al., 1994; Van Cappellen et al., 2002; Fraysse et al., 2009). In a controlled, 6-week-long partial dissolution study, Cabanes and Shahack-Gross (2015) found that small morphotypes such as rondels and bilobates (GSSCs), and large bulliforms were

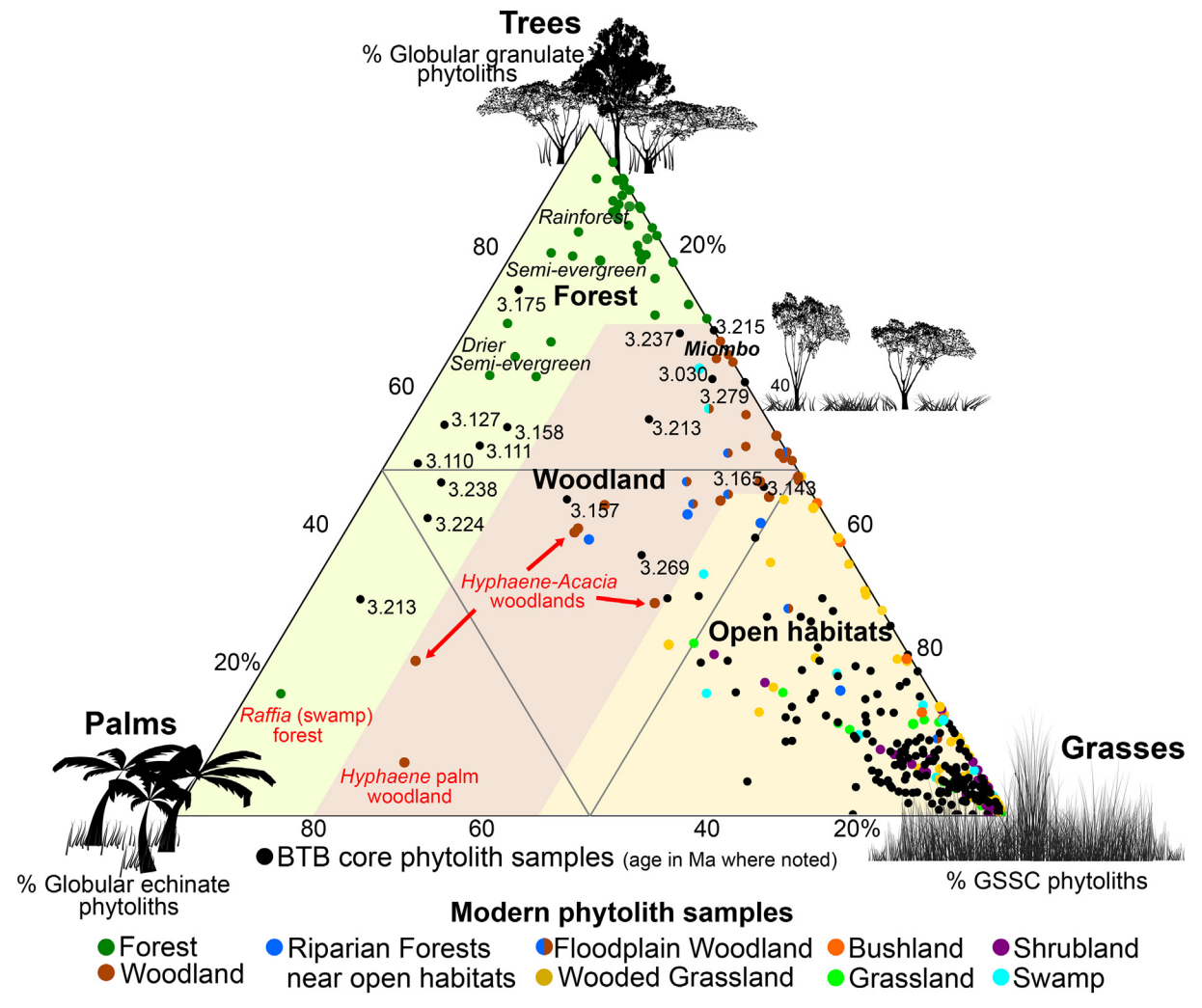


Fig. 7. Ternary plot for the percentages of palm (Arecaceae), tree (dicotyledonous/ligneous), and grass short cell (GSSC; Poaceae) phytolith indicators (A:D:P) from 168 western, central, and eastern African modern soils (colored dots), plotted with A:D:P values for samples from BTB13 (black dots). The modern values were calculated from published phytolith counts (SOM Table S2) and then colour coded by vegetation formation after White (1983). Shaded vegetation formation type regions are based on the modern samples. BTB13 samples older than 3.0 Ma that plot within a forest or woodland region are labeled with their respective age. The moderate to high percentages of palm phytoliths in these pre-3.0 Ma BTB13 samples indicate an affinity with groundwater-fed woodlands and forests.

more resistant to dissolution than many other morphotypes. However, when just looking at GSSCs and bulliform phytoliths from their study, the absolute abundance of bilobates from the grass Oryza sativa was reduced ~55% after partial dissolution, while bulliform abundance was unchanged within the margins of error. Thus, when exposed to high pH water over a long period of time, bulliform phytoliths may still be recognizable, but severely eroded, whereas GSSC and globular arboreal phytoliths may have dissolved to unrecognizable forms because of their relatively small volume. Our observations agree with the Cabanes and Shahack-Gross (2015) conclusion that under conditions of partial dissolution, bulliforms may be overrepresented. However, Novello et al. (2012) showed that surface soil samples in a swamp dominated by reeds (Typha) and grasses (Vossia, Phragmites) produced a phytolith assemblage with < 1% GSSCs, and 99% bulliform, elongates, and trichomes. Thus, the absence or rarity of GSSC phytoliths is not always an indicator of dissolution, especially if bulliforms are well preserved.

5.1.2. Biogenic silica replacement/re-precipitation

A type of biogenic silica replacement and/or re-precipitation has also been observed in BTB13 sediments where the opal silica matrix is partially or fully replaced and voids are infilled by crystalline material (Figs. 11 and 5.14–5.15). This replacement process is consistent with

diatom frustule aluminosilicate replacement observed in near-shore marine deltaic anoxic muds (Michalopoulos et al., 2000; Michalopoulos and Aller, 2004; Derkowski et al., 2015) and saline-alkaline Bolivian lakes from the Altiplano (Badaut and Risacher, 1983). Arráiz et al. (2017) observed the growth of zeolites on phytoliths from early Pleistocene sediments at Olduvai Gorge, Tanzania. In a controlled dissolution study by Prentice and Webb (2016), evidence for re-precipitation of silica on phytolith surfaces was observed when silica saturation was above 30–40%. Sediment pore water silica saturation in combination with alkaline (high pH) conditions may play a role in the replacement/re-precipitation alteration of biogenic silica observed in BTB13, as was observed in lakes from the South American Altiplano (Badaut and Risacher, 1983).

5.2. Sponge spherasters and the potential for phytolith misidentifications

Sponges are notable in their ability to tolerate conditions above pH 8, as many African taxa inhabit lakes in the pH 8 to 9 range (Manconi and Pronzato, 2009). *Dosilia brouni* was collected in 1979 from Lake Baringo when it had a measured salinity of 0.5% and a pH of 8.4 (Vacelet et al., 1991), indicating its tolerance of saline and basic conditions. The possible recovery of *Dosilia brouni* in BTB13 may

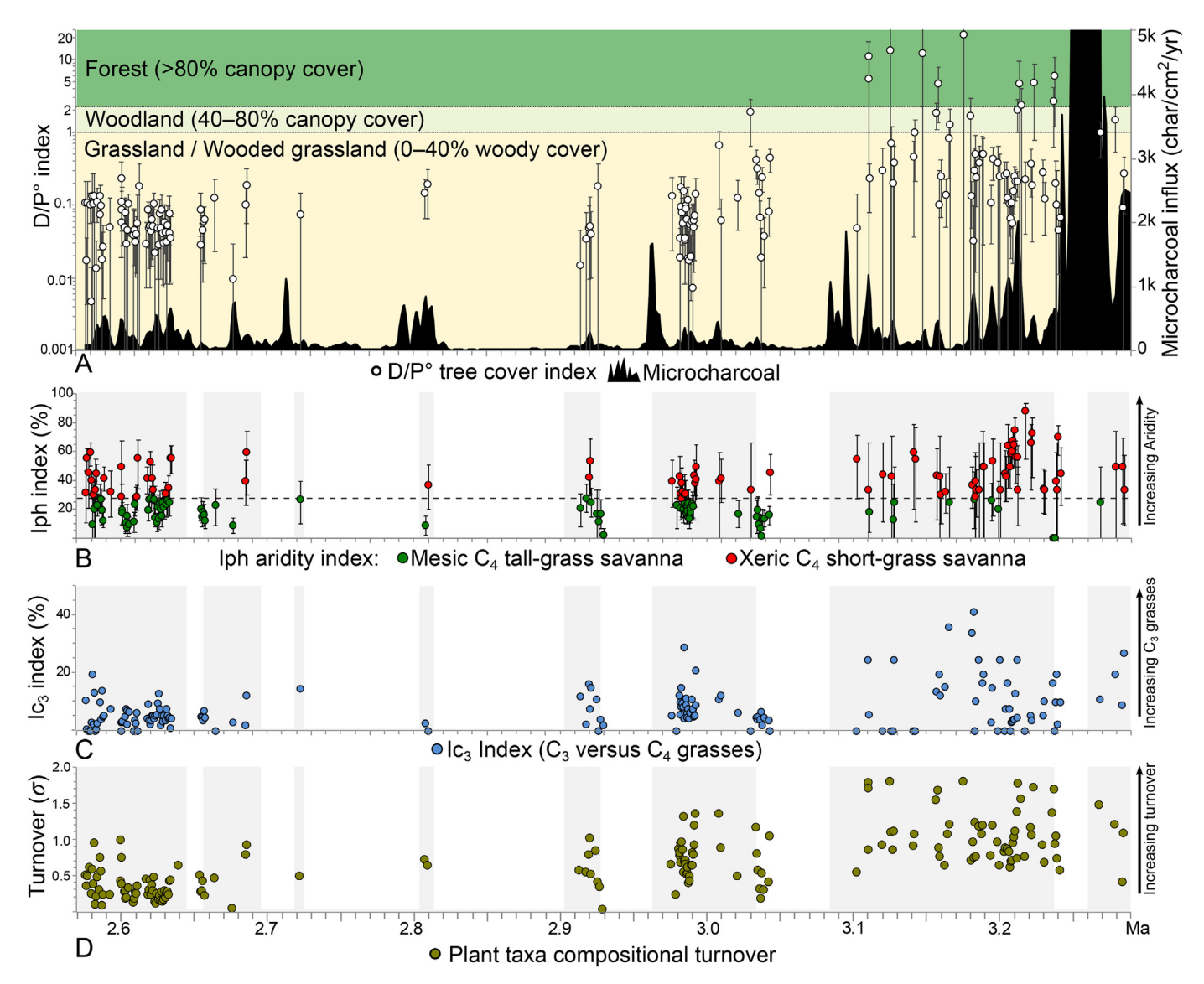


Fig. 8. Phytolith indices for tree cover, aridity, C_3 vs. C_4 grasses, and plant taxa compositional turnover. A) D/P° phytolith index for tree cover and 10-kyr Gaussian smoothed microcharcoal influx. D/P° values 0–1 indicate open grassland, shrubland, or wooded grassland with < 40% woody cover. D/P° values of 1–2.2 indicate woodland with 40–80% woody cover. D/P° values > 2.2 indicate forest with 80–100% woody cover (Fig. 6). Nonparametric bootstrap resampling was used to calculate the 95% confidence intervals. B) Iph phytolith index for aridity. A value of 27.8% from Novello et al. (2017) separates mesic tall-grass Sudanian from xeric short-grass Sahelian communities (horizontal dashed line). Iph values ≤ 27.8% may indicate MAP > 750 mm. Nonparametric bootstrap resampling was used to calculate the 95% confidence intervals. C) Ic₃ phytolith index for the percentage of C₃ short cell phytoliths relative to the sum of all C₃ and C₄ short cell phytoliths. D) Plant taxa compositional turnover index in units of standard deviation. Turnover was estimated using detrended canonical correspondence analysis (DCCA; Birks, 2007). Higher values indicate greater plant taxa compositional turnover in adjacent samples.

suggest a prior hydrologic connection to its type locality in the Nile River system (Vacelet et al., 1991; Stewart, 2009), or simply a wider distribution for this taxon in the past. In BTB13, sponge concentrations peaked as lakes were either transgressing from highly evaporative (high alkalinity/pH) states or regressing from higher lake level (low alkalinity/pH) states (Fig. 3H).

When pH was interpreted as increasing in the BTB13 core, sponge spherasters were often the last BSi fossils to remain. Spherasters, a type of sponge microsclere (Boury-Esnault and Rützler, 1997), are produced by some, but not all freshwater and marine sponges (e.g., Łukowiak et al., 2013; Łukowiak, 2016), and have been observed in modern lake sediments from temperate North America (Yost et al., 2013). For Africa, spherasters have been described for the tropical and equatorial taxa *Corvospongilla boehmii*, and *C. micramphidiscoides* (Manconi and Pronzato, 2009).

Spherasters are strikingly similar to globular echinate phytoliths

produced by palms (Arecaceae); however, they have a sub-micron pore-like opening that is usually visible on the centrum or a spine (Fig. 5). As dissolution progresses, the diameter of the opening increases and the echinate projections become diminished (Fig. 11). Under conditions of silica replacement or re-precipitation, the opening can fill in. As diagenesis proceeds, the spheraster may come to resemble a globular phytolith morphotype associated with woody plants. The main implication is that globular echinates must be fully rotated to rule out the presence of a pore-like opening before being interpreted as a palm phytolith. To our knowledge, and with the exception of Yost et al. (2013, 2018), sponge spherasters have not been reported in published phytolith paleoecological studies, raising a concern that palms may have been misidentified in some of those studies.

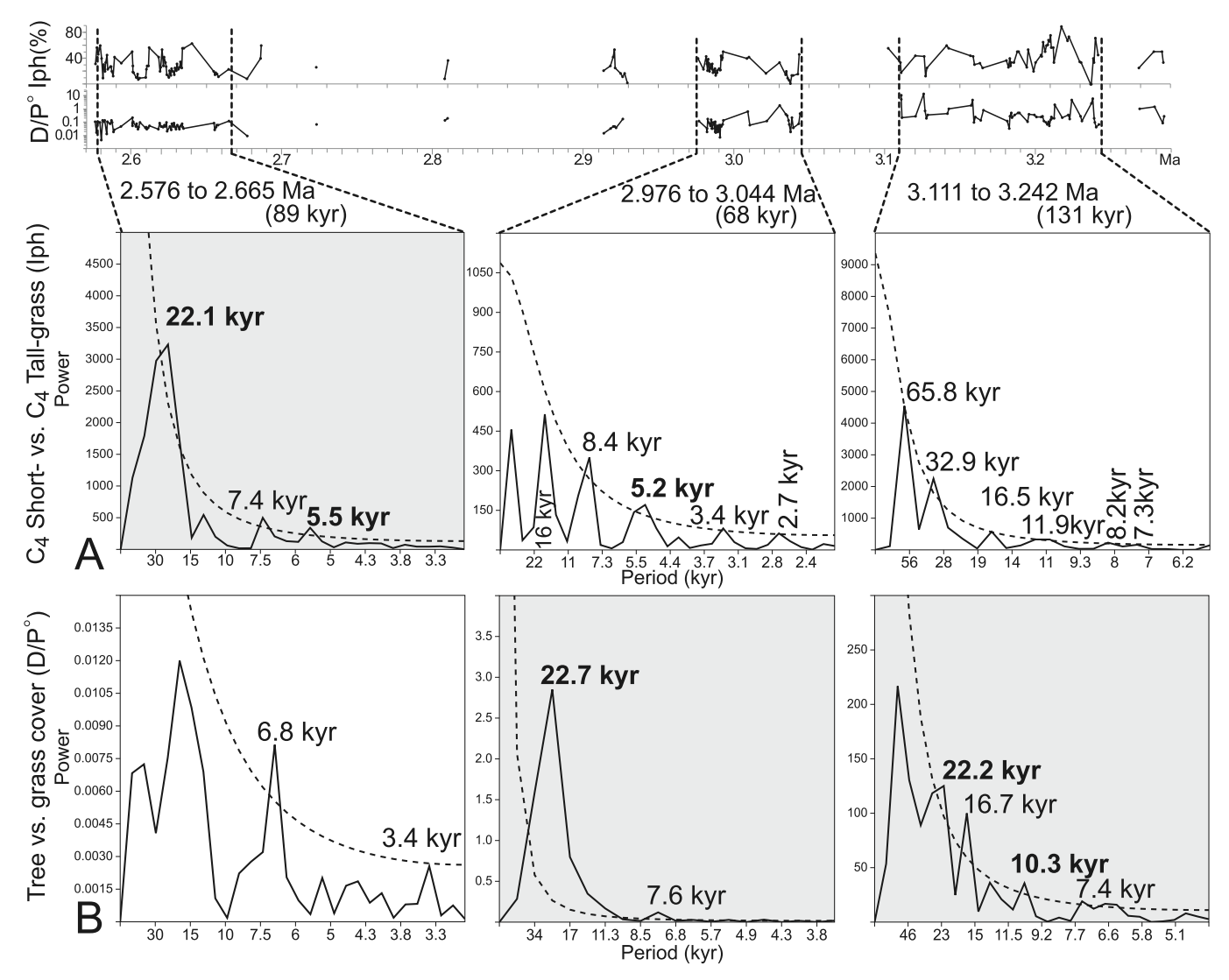


Fig. 9. REDFIT spectral analysis of Iph and D/P $^{\circ}$ phytolith indices for three time-intervals from BTB13 with good phytolith preservation. Spectra with gray backgrounds have precession periodicities (19–23 kyr). Precession and sub-precession periodicity peaks are in bold. Dashed lines represent 95% confidence levels. A) Iph aridity index for xeric C₄ short-grass vs. mesic C₄ tall-grass abundance. B) D/P $^{\circ}$ index for tree vs. grass cover abundance. Tree vs. grass dynamics exhibit precession periodicity before \sim 3.0 Ma and short- vs. tall-grass dynamics exhibit precession periodicity after \sim 3.0 Ma.

5.3. Recognition of biased phytolith assemblages

Of the 652 phytolith samples analyzed, 48% exhibited evidence of moderate to severe dissolution and probable morphotype preservation bias. To avoid skewed and misleading results, D/P°, Iph, and Ic₃ phytolith indices were not calculated from potentially biased samples (Figs. 2 and 3F). For example, given the diagenetic transformation of sponge spherasters and palm globular echinate phytoliths to appear as globular granulate tree phytoliths, tree cover calculations could have been grossly overestimated in the biased samples.

5.4. Phytoliths identify ecologically diagnostic plants

5.4.1. Dayflower (Commelina spp.)

At least two species of *Commelina* (dayflower) were identified from the phytolith record (Table 2; Figs. 3D and 4). *Commelina* spp. are a common agricultural weed in Africa (Eichhorn et al., 2010), but are also an important component of undisturbed plant communities. Over 23 species are listed for the highlands of Kenya, with seven occurring in Baringo County (Agnew, 2013). Although some species in Kenya occur in dry grasslands, most are associated with wet soils in grasslands,

woodlands, and forests. The highest abundances of *Commelina* phytoliths, and in particular *C. diffusa*-type phytoliths, occurred before 3.10 Ma (Fig. 3D). *C. diffusa* is found today at the edges of swamps, riverbanks, and wet forests (Agnew, 2013). *Commelina* is eaten by African primates, including lowland gorillas, monkeys, and chimpanzees (Mitani et al., 1993; Huffman et al., 1997; Isbell, 1998).

5.4.2. Riverweed (Tristicha trifaria, Podostemaceae)

Because riverweeds have an extremely narrow habitat niche, their phytoliths are an indicator of stream flow gradients and precipitation change. Riverweeds (Podostemaceae) are a family of aquatic plants restricted to flat rocks in rapids and waterfalls, especially on the rims, where they are seasonally submerged by oligotrophic waters and exposed during dry seasons (Müller et al., 2003; Koi et al., 2015). There are three Podostemaceae genera in Kenya, each with only one species. The Podostemaceae phytoliths recovered here are a good match with *Tristicha trifaria* (da Costa et al., 2018)(Fig. 4), which occurs today in Baringo County above 1300 m elevation (Agnew, 2013). For the other two Kenyan genera, *Ledermanniella* does not produce phytoliths (Ameka et al., 2003), and production in *Sphaerothylax* is unknown.

Riverweeds only appear in the BTB13 record after 3.04 Ma

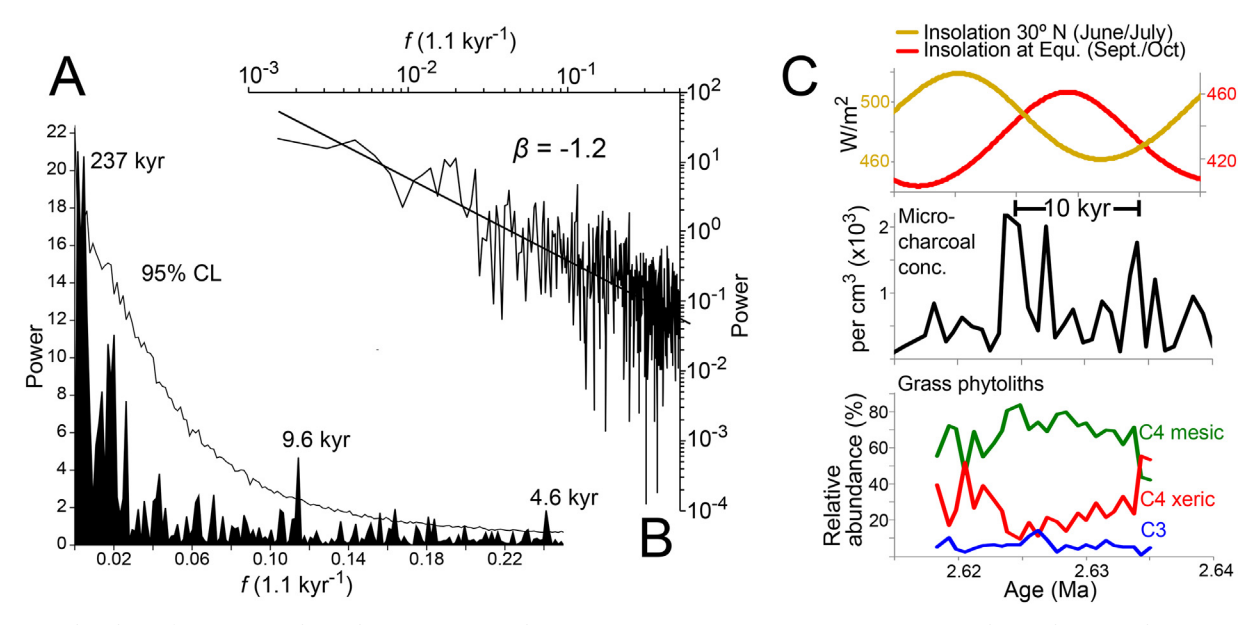


Fig. 10. Spectral analysis of BTB13 microcharcoal concentrations and comparison to grass community composition. A) Lomb periodogram with a Monte Carlo 95% confidence level (CL). B) Power spectral density plot of the Lomb periodogram (Log power vs. Log frequency) with slope ($\beta = -1.2$) derived from a least squares regression. C) Records of insolation (Laskar et al., 2004), microcharcoal, and C_3/C_4 grass phytoliths for a 20 kyr interval centered at 2.627 Ma. Peaks in microcharcoal 5 kyr before and after an insolation maximum are likely the source of the half-precessional periodicity. Peaks in mesic C_4 grass phytoliths correspond to peaks in insolation, indicating enhanced monsoon precipitation during insolation maxima.

(Fig. 3C), indicating either an increase in seasonal precipitation or a change in basin morphology and sediment sourcing. It should be noted that there is a BSi dissolution zone between ~ 3.10 and 3.04 Ma, so if riverweeds were on the landscape during that time, their phytoliths would not have been preserved. Prior to ~ 3.10 Ma, sediments may have been delivered by low gradient rivers. After ~ 3.10 Ma,

reconfiguration of the hydrology could have resulted in sediment delivery from higher elevation source areas. Peaks in riverweed abundance are coincident with insolation peaks, indicating enhanced monsoonal precipitation and inflow to the basin during insolation maxima (Prell and Kutzbach, 1987; Tuenter et al., 2003; Kutzbach et al., 2020).

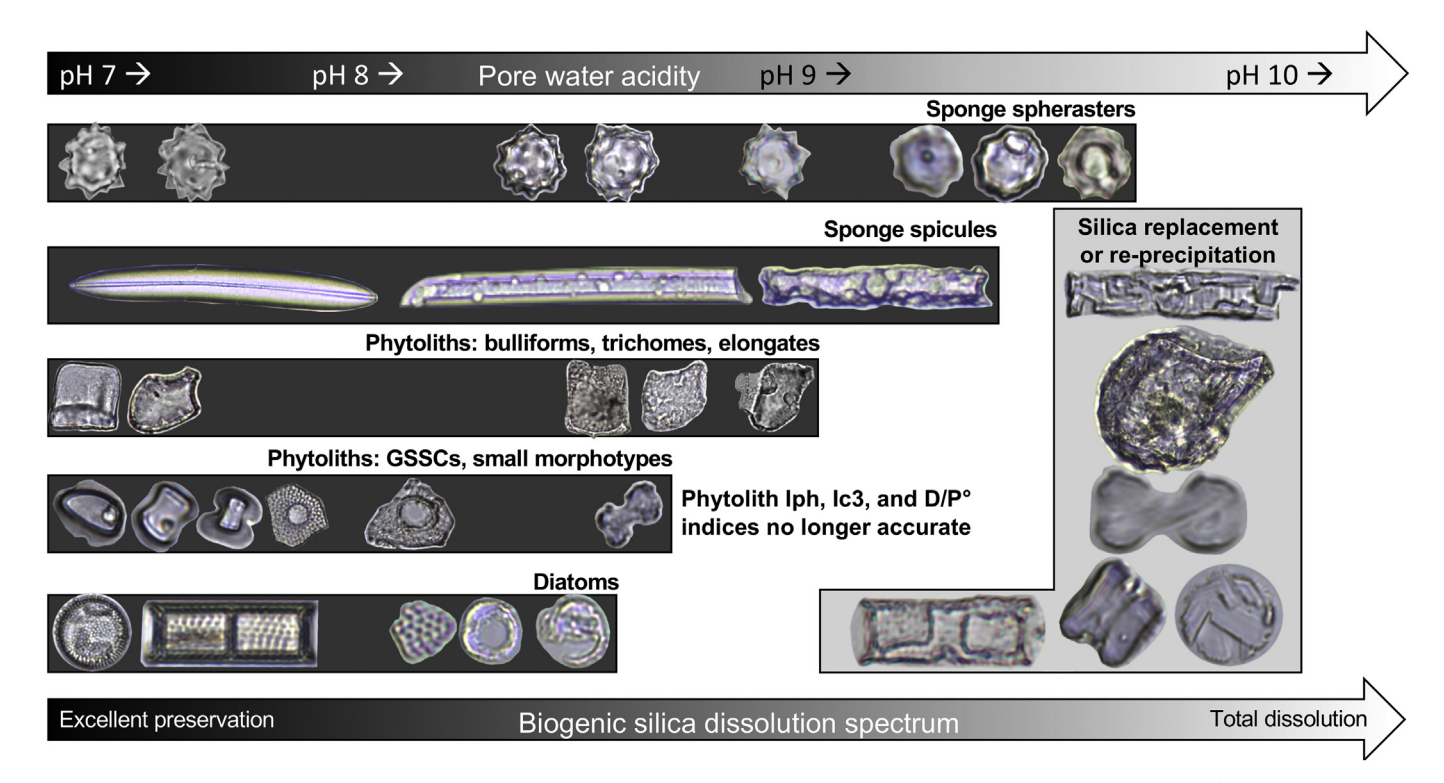


Fig. 11. Conceptual model for the biogenic silica dissolution succession (black bars) and silica replacement or re-precipitation (gray box) observed in BTB13 under increasing pore water pH. The dissolution model approximates the pH at which various microfossils disappear from the record relative to the others as pH increases. Images of pristine to degraded microfossils (left to right) illustrate how biogenic silica dissolution and diagenesis is typically observed using transmitted-light microscopy. Occasionally, microfossils exhibiting evidence of silica replacement or re-precipitation of crystalline silica are observed.

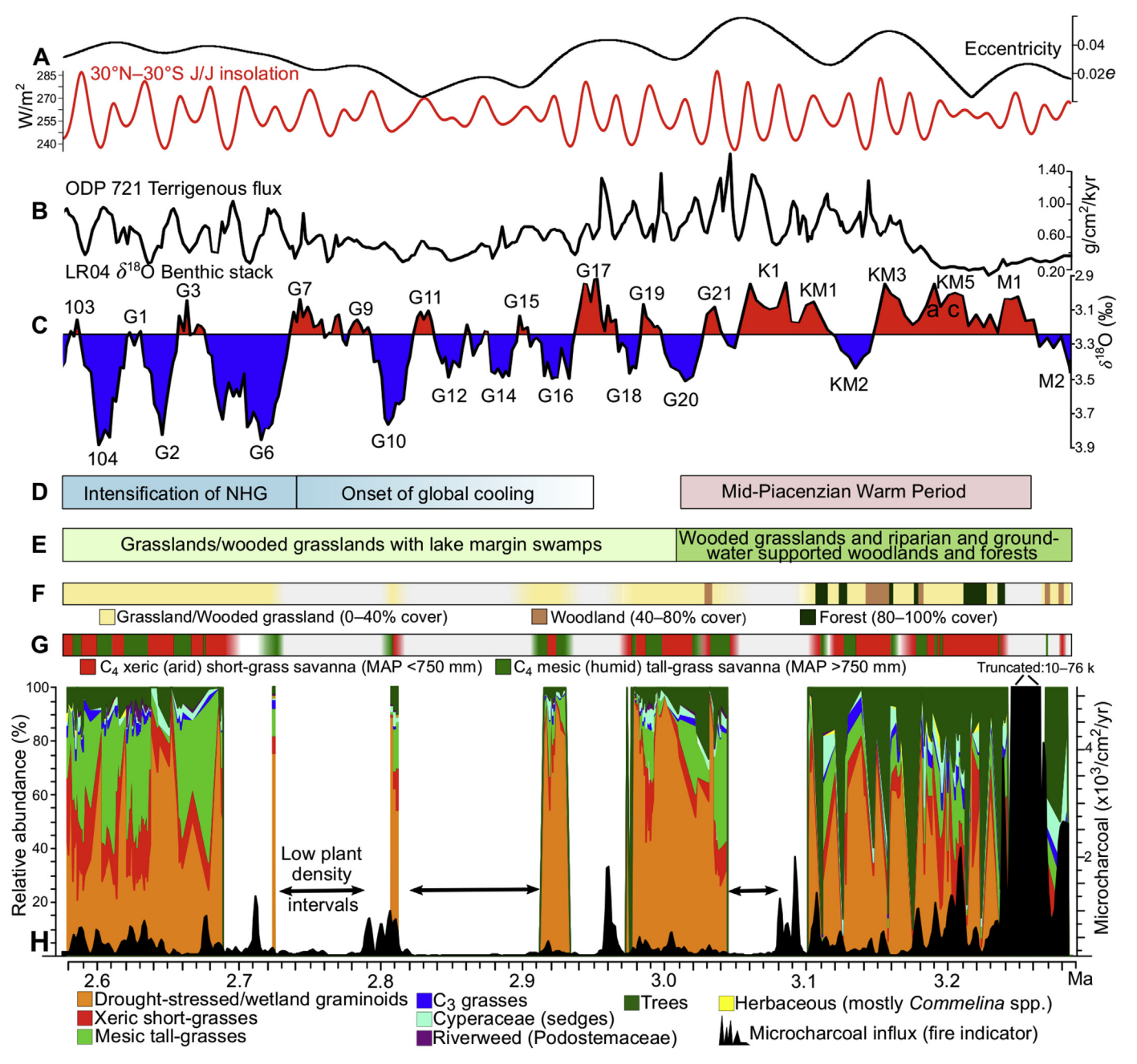


Fig. 12. Vegetation and charcoal summary with comparison to selected regional and global climate records. A) June/July 30° N to 30° S insolation gradient and eccentricity (Laskar et al., 2004). B) Terrigenous (dust) flux from Arabian Sea ODP site 721/722 (deMenocal, 1995). C) LR04 global benthic δ^{18} O stack (Lisiecki and Raymo, 2005) with the horizontal line = 3.25‰ (avg. last 5 kyr of Holocene) dividing marine isotope stage glacials (blue) from interglacials (red). D) Global climate events. E) Summarized BTB13 core vegetation formation reconstruction. F) Percent tree canopy cover reconstruction based on a modern African dataset of D/P° phytolith index values and the White (1983) vegetation formation classification for Africa. G) Arid short-grass versus humid tall-grass savanna reconstruction based on the Iph phytolith index. H) Phytolith morphotype-based percentages of plant functional types (Table 1), plotted with 10-kyr Gaussian smoothed microcharcoal influx values. White intervals indicate periods with partial to complete phytolith dissolution due to high soil/sediment pore water pH. Black arrows indicate intervals when upland plant densities may have been too low to carry fire on the landscape. (For interpretation of the references to colour in this figure legend, the reader is referred to the web version of this article.)

6. Paleoenvironmental reconstructions

The combined pollen, phytolith, and microcharcoal datasets are used here to reconstruct the vegetation and fire history of the paleolake Baringo catchment from 3.29 to 2.58 Ma (Fig. 12). Discussion is organized by the phytolith preservation zones depicted in Fig. 3.

6.1. Zone 1: 3.29 to 3.10 Ma

Zone 1 represents the bottom of the core at 3.29 Ma (\sim 228 mbs) to 3.10 Ma (\sim 152 mbs). This interval captures the last half of the marine isotope stage (MIS) M2 global cooling event (\sim 3.31–3.26 Ma; De Schepper et al., 2014), which caused cooler and wetter conditions in eastern Africa (Bonnefille et al., 2004; Dolan et al., 2015; Tan et al., 2017), and the first two-thirds of the MPWP (3.26–3.01 Ma), when global surface temperatures were 3 $^{\circ}$ to 4 $^{\circ}$ C warmer than modern,

atmospheric *p*CO₂ was similar to modern values, and models and paleodata indicate tropical savannas, woodlands, and forests expanded in Africa at the expense of drier biomes (Salzmann et al., 2008; Haywood et al., 2016). The MPWP is often used as an analog for future global warming (Salzmann et al., 2009; Salzmann et al., 2011).

The pollen and phytolith records in the BTB13 core both indicate that woodlands and forests were more widespread compared to later in the record, particularly during the MPWP. This finding supports reconstructions based on vegetation models and paleodata referenced above, and the BTB13 leaf wax isotopic record (Lupien et al., 2020). Pollen presence/absence data recorded the occurrence of typically high elevation afromontane trees (particularly *Podocarpus*), mid-elevation montane forests, and dry lowland forests in close temporal proximity. Although the presence of tree taxa that occur today in the higher elevations under cooler temperatures could be interpreted as representing the existence of montane forests near the lake during this time, recent work has shown that many montane species' ranges are more constrained by moisture than by cooler temperatures (Ivory et al., 2016; Ivory et al., 2018). In either case, this suggests the existence of heterogeneous but largely arboreal mesic to seasonally dry vegetation during these times.

The phytolith record, which is a more localized proxy than pollen, indicates oscillations between open savanna (< 40% woody cover), woodland (40–80% cover) and forest (80–100% woody cover) formations (Figs. 8 and 12). Peaks in microcharcoal concentrations are antiphased with the woodland and forest occurrences. The highest levels of plant taxa compositional turnover for BTB13 was observed in Zone 1. Arid short-grass savanna and woodlands prevailed during MIS M2, and fire frequency was at its highest levels observed for the core, particularly during the transition from MIS M2 to the MPWP, when microcharcoal concentrations were $14 \times$ the BTB13 average. Extremely large microcharcoal peaks (truncated in Figs. 8 and 12), may point to catastrophic stand-replacing fires within the watershed. This data supports phylogenetic evidence that the late Pliocene was a peak period for the evolution of fire-adapted woody clades in Africa (Bond, 2015).

Forests with > 80% woody cover appear in the phytolith record during the MPWP, but were relatively short lived (\sim 10 kyr), and often transition to or from woodlands or savanna within 0.5 to 1 kyr. Many of the woodland and forest phytolith assemblages have a significant proportion of palm phytoliths, and comparisons to modern samples (Fig. 7) suggest these may primarily be groundwater-supported riparian settings. It is possible that the relatively rapid transitions between these vegetation types were caused by riverine corridor migration at or near the BTB13 drill site.

6.1.1. Mesic C_3 -xeric C_4 hydroclimate paradox

Trees (including palms), C_3 grasses, and sedges, sometimes occurring in very high percentages and generally indicative of more mesic conditions, are most prevalent within Zone 1; yet at the same time, xeric C_4 grass dominance occurs more often than mesic C_4 grass dominance (Figs. 8 and 12). This could signal that C_3 trees and C_3 grasses were maintained by groundwater along a riverine corridor, or that the short-grass/tall-grass dynamic was decoupled from climate, as can happen when grazing lawns are created under high herbivore pressure (McNaughton, 1983). However, comparison of phytolith preservation zones to the summer insolation curve shows that before ~ 3.10 Ma, phytoliths were best preserved at insolation minima and during periods with low amplitude insolation maxima; after ~ 3.10 Ma they were best preserved during insolation maxima (Fig. 3).

Based on the absence of deep lake phases and the prevalence of shallow lacustrine, floodplain, wetland (gleyed soils), and deltaic deposits before ~ 3.10 Ma (Scott et al., 2020; Westover et al., 2020), a conceptual phytolith preservation model is depicted in Fig. 13. Before ~ 3.10 Ma, enhanced precipitation during insolation maxima raises the elevation of high pH lake water above that of the drill site, resulting poor to no phytolith preservation. Because of the more proximal

position of the drill site within a relatively shallow basin, reduced precipitation during insolation minima (and dampened insolation maxima) reduces the elevation of high pH lake water below that of the drill site, resulting in exposure to only relatively less saline/alkaline shallow groundwater and surface seeps, springs, and streams, and thus much better phytolith preservation. Similar scenarios of high pH lake water being drawn down during periods of low precipitation, exposing freshwater features and habitats has been documented on orbital time scales for the Bonneville Basin in Utah (Balch et al., 2005) and the Olduvai Basin in Tanzania (Ashley et al., 2009). Some of the well-preserved phytolith extracts within this zone included phillipsite crystals in the extractions that were either inherited from the substrate or transported to the drill site from adjacent areas.

For the conceptual model after ~ 3.10 Ma (Fig. 13), accommodation in the basin increased, allowing for deeper lakes during periods of high insolation and enhanced precipitation. The presence of riverweed (Podostemaceae) starting at 3.04 Ma (Fig. 3C) is evidence that steep gradient streams and rivers were established and delivering oligotrophic water into the basin. This would have diluted alkaline (high pH) lake water formerly present during periods of high insolation, allowing for good phytolith preservation. Phytoliths recovered during peak insolation after 3.10 Ma were typically well-preserved, suggesting neutral or even slightly acidic lake water pH. During periods of reduced precipitation (insolation minima and dampened insolation maxima), lake water increased in salinity and alkalinity/pH, as evidenced by the precipitation of sodic zeolites (Fig. 3F), but lake levels were not low enough to expose sediments to fresh groundwater or meteoric water, precluding phytolith preservation.

The phytolith preservation model depicted in Fig. 13 implies that prior to 3.10 Ma, phytoliths would be recording vegetation primarily during periods of decreased precipitation, and after 3.10 Ma, they would be recording vegetation primarily during periods of increased precipitation. This is in fact what we see in the grass phytolith record (Fig. 12G). However, there is a short interval centered around 3.20 Ma (204–190 mbs) when phytoliths were preserved during two probable humid periods consisting of two insolation maxima, one high- and one low-amplitude (Fig. 14). As observed elsewhere in the core, xeric C4 grasses are dominant during insolation minima and dampened insolation maxima, and mesic C4 grasses are dominant during prominent insolation maxima.

6.2. Zone 2: 3.10 to 3.04 Ma

Zone 2 spans from 3.10 Ma (\sim 152 mbs) to 3.04 Ma (\sim 132 mbs), encompassing the MIS K1 interglacial. Poor phytolith preservation, resulting in biased and sometimes no phytolith recovery, precluded vegetation reconstructions. There is a peak in phytolith concentrations coincident with a peak insolation at 3.08 Ma; however, pore water conditions were apparently still too basic for smaller phytoliths to be preserved. High microcharcoal concentrations and influx at the beginning of K1 followed by very low values for the remainder of K1 and through G21 suggests that catastrophic fires followed by drought may have drastically reduced woody vegetation on the landscape. Climate model simulations indicate that K1 was a much warmer event than KM5c in Africa (Prescott et al., 2014).

6.3. Zone 3: 3.04 to 2.91 Ma

Zone 3 spans 3.04 Ma (\sim 132 mbs) to 2.91 Ma (\sim 100 mbs) and occurs during the last half of a 300 kyr interval with high eccentricity. The highest 30° N to 30° S summer insolation gradient value for BTB13 (284 w/m²) occurred at 3.037 Ma (Fig. 3F; see SOM Fig. S1), which coincides with well-preserved phytolith samples and the deposition of the oldest of the thick Barsemoi outcrop diatomites, "D0", identified by Deino et al. (2006) and recently described as Diatomite Interval 1 by Westover et al. (2020).

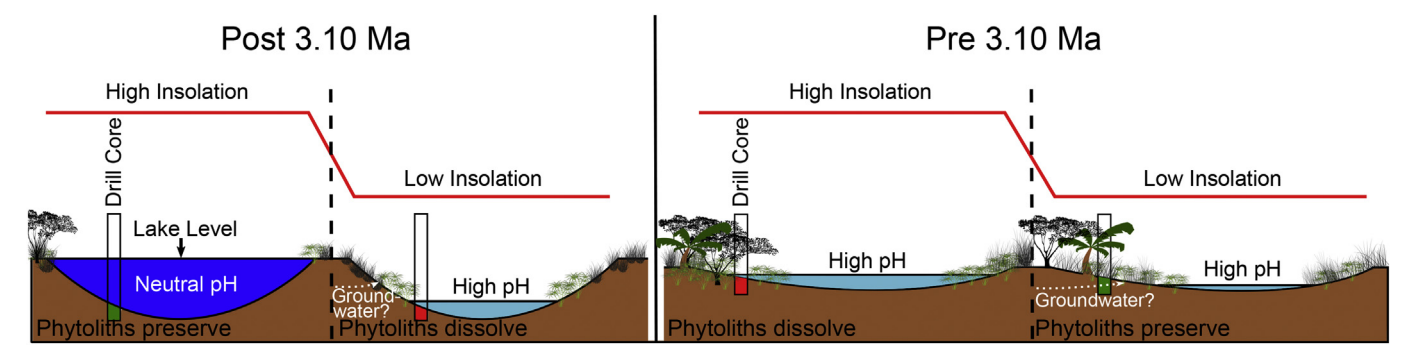


Fig. 13. Conceptual model for the changing relationship between insolation, BTB13 lake water pH, and phytolith preservation before and after 3.10 Ma. Lake levels and basin morphologies are not to scale and only illustrate relative differences between time periods. Pre-3.10 Ma lithologies include sediments indicative of lacustrine, riverine, wetland, and deltaic facies.

Another peak in the 30° N to 30° S summer insolation gradient occurs between 2.993 and 2.981 Ma (117.13–114.66 mbs), where the highest phytolith concentrations for the core were observed (mean for interval = 1.4×10^6 per cm³, maximum = 6.8×10^6). In fact, for a few samples between ~117–116 mbs, phytoliths comprised ~30% of smear slide particles (unprocessed lake sediments smeared on microscope slides). This suggests the presence of a near-shore, emergent aquatic vegetation habitat with near-neutral pH water for a portion of this ~1 m interval, which impeded siliciclastic sediment dilution, and from which most of the original organic matter decayed, leaving a phytolith concentrate. Modern sediments with similar high phytolith abundances have been observed from the Ngoitokitok wetland, Ngorongoro Basin, Tanzania (Deocampo and Ashley, 1999).

This zone contains a third interval with good phytolith preservation and high phytolith concentrations that also coincides with a peak in the 30° N to 30° S summer insolation gradient at \sim 2.92 Ma. However, there is a very prominent insolation gradient peak at \sim 2.94 Ma that does not correspond with a zone of good phytolith preservation. This is the same region of BTB13 where Deino et al. (2020) suggest that there may be a \sim 40 kyr depositional hiatus. Thus, sediments associated with the insolation gradient peak at \sim 2.94 may not have been recovered, or the

phytolith concentration peak at 2.92 Ma may actually be associated with the 2.94 Ma insolation gradient peak.

Other than the brief appearance of woodland vegetation at 3.03 Ma, vegetation during this zone had transitioned to savanna and was unlikely to have had more than 40% tree cover. Phytoliths diagnostic of woody taxa generally decrease over time across the zone. Very high percentages of bulliform grass phytoliths, as well as riparian indicators suggest the presence of a swamp at or near to the drill site (Fig. 12). No tree pollen was observed, but one sample yielded grass pollen (Fig. 3*G*).

For the upland grass community, short-grass/tall-grass dynamics appear to be mediated by insolation, whereby mesic C_4 tall-grasses become dominant during periods of high summer insolation in response to increased (presumably monsoonal) precipitation. Iph values $\leq 27.8\%$ may indicate MAP in excess of 750 mm (Fig. 8). Riverweed (*Tristicha trifaria*, Podostemaceae) appeared for the first time in the BTB13 record in Zone 3, and its abundance also appears to peak during insolation maxima (Fig. 3C). This suggests that either basin morphology changed towards steeper gradients, allowing for more rapidly flowing oligotrophic waters over rocky substrates to enter into the basin, or there was simply more precipitation that allowed for spillover of oligotrophic waters from higher elevations.

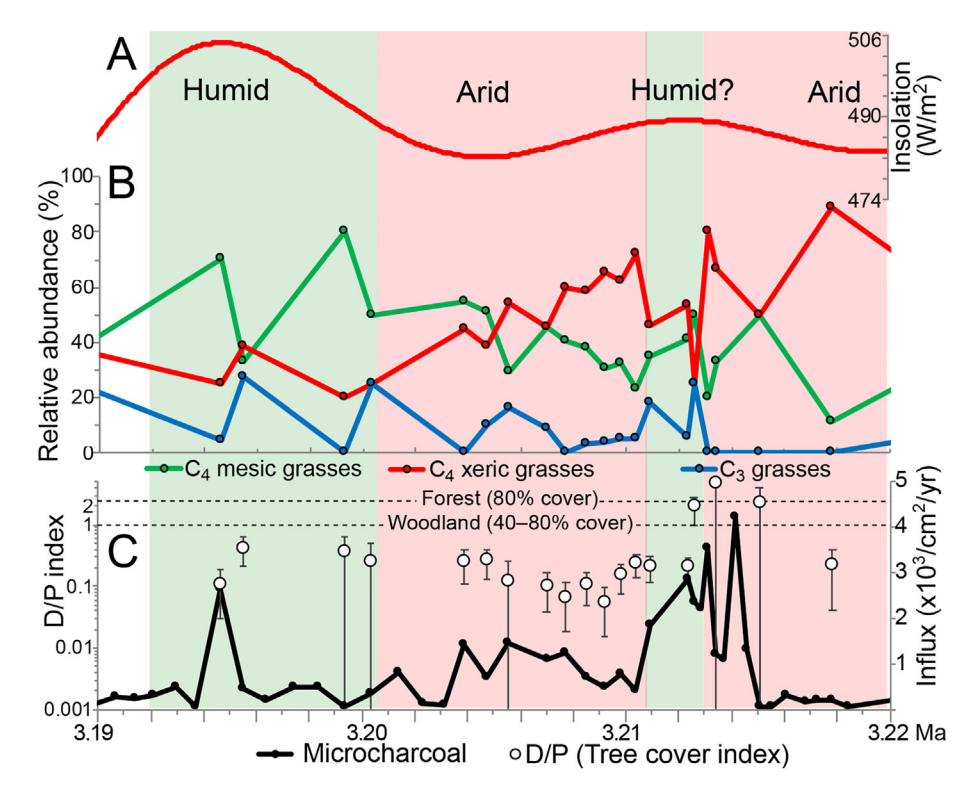


Fig. 14. Grass, tree cover, and microcharcoal from 3.218 to 3.190 Ma. A) Summer insolation at 30° N with one prominent and one dampened insolation maximum and two insolation minima (Laskar et al., 2004). B) Percentages of C_4 mesic, C_4 xeric, and C_3 grass phytoliths. C) Microcharcoal influx and D/P° tree cover index. Despite inherent uncertainties in the age model, there is generally good agreement between the insolation curve and vegetation response to changes in the inferred hydroclimate.

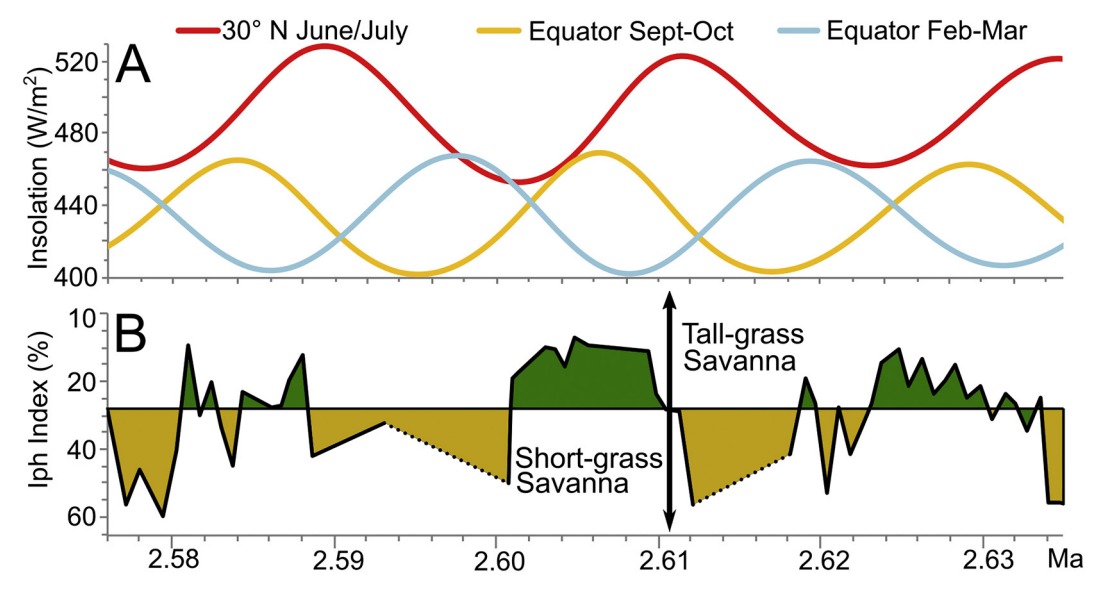


Fig. 15. Comparison of insolation and tall-grass vs. short-grass savanna dominance for the uppermost portion of BTB13. A) Seasonal insolation curves for boreal spring, summer, and fall (Laskar et al., 2004). B) Iph index values below 27.8% indicate the presence of tall-grass savanna. Dashed-lines denote intervals with poor phytolith preservation and no Iph values calculated.

Microcharcoal concentrations tend to peak ~ 5 kyr before and after peaks in insolation, similar to what is depicted in Fig. 10C, resulting in double charcoal peaks along the shoulders of an insolation peak. This ties insolation to a 10 kyr periodicity in increased fire frequency. Fire frequency in African savannas is positively correlated with annual precipitation (Lehmann et al., 2014). In eastern Africa, fire-adapted C_4 mesic tall-grasses (Simpson et al., 2016) dominate the herbaceous layer when MAP crosses an approximately ~ 750 mm threshold (McNaughton, 1983). It appears that fire regimes, C_4 tall-grass Panicoideae abundance, and precipitation variability, as observed here in the BTB13 core are all influenced by eccentricity modulated peaks in insolation at precessional periodicity.

Lastly, MIS G17 interglacial (Fig. 12) appears to have been a time of significantly decreased effective moisture in the Baringo Basin, as phytolith dissolution indicates high sediment pore water pH, and very low microcharcoal concentrations suggest vegetation density was too low to carry fire. Relatively high peaks in microcharcoal at over four times the mean were observed at the onset of G17, similar to that observed for the onset of the K1 interglacial. Since woody cover was already much reduced by this time, these significant fire events could be derived from fires occurring in higher elevation forests. Humic acid content was also high during G17 indicating the presence of soils or shallow wetlands at the core site (Fig. 31).

In summary, these results suggest that precession has an influence on equatorial vegetation and fire dynamics, a unique finding that validates similar modeled results (Tuenter et al., 2003). Comparison of our results with the 30° N to 30° S insolation gradient curve also indicates that cross-equatorial advection of heat and moisture may enhance or modulate eastern African precipitation, in agreement with similar findings from southern Kenya (Verschuren et al., 2009) and Asia (Beck et al., 2018).

6.4. Zone 4: 2.91 to 2.72 Ma

Zone 4 spans from 2.91 Ma (\sim 100 mbs) to 2.72 Ma (\sim 75 mbs), and is characterized by no pollen, the nearly complete absence of well-preserved phytoliths, and relatively low charcoal concentrations, suggesting that plant densities were typically too low for fire transmission across the landscape (Figs. 3*J* and 12*H*). Regarding the drivers of fire in southern Africa, Archibald et al. (2009) found that fire was rare in areas with MAP < 288 mm. This zone coincides with an interval of

particularly low eccentricity, when normally strong 100 kyr periodicity almost disappeared. Berger and Loutre (1991) note that this also occurred between 4.8 and 4.4 Ma and that these are unique features in the time evolution of eccentricity over the last 5 Ma. Zone 4 is subdivided into two 100 kyr intervals, 4a and 4b, which are separated by an approximately 2000 yr interval (88.47 to 88.14 mbs) with good phytolith and diatom preservation, and coeval with peak MIS G10 glacial cooling (Fig. 12). There were no zeolites or calcic minerals within this phytolith/diatom interval, but there are sodic zeolites above and below (Fig. 3F). The middle portion of Zone 4a coincides with Mineral Zones 3 and 4 from Minkara et al. (2020), which was virtually zeolite free, possibly because of unsustained inflow of solutes.

The well-preserved phytolith samples at \sim 88 mbs (2.81 Ma) indicate that during the MIS G10 glacial, precipitation increased significantly. Fire also returned to the landscape during this interval and for 20 kyr afterwards. There was likely an herbaceous swamp near the drill site. The Iph index indicates that tall-grass savanna was in place for part of this interval in the uplands, and this suggests that MAP may have been near or above 750 mm. However, there is no evidence that woody cover increased, suggesting the length of dry season must have remained long (> 6–7 months; Hély et al., 2006). Preserved diatoms from this same interval indicate the presence of a relatively deep, and well-mixed lake (Westover et al., 2020).

Zone 4b (\sim 88–75 mbs) spans the MIS G9 to G7 interglacial interval and also corresponds with Mineral Zone 5 from Minkara et al. (2020), which they describe as the most sustained episode of aridity and salinity for the core. No pollen was observed, presumably from repeated wetting and drying, and phytoliths were either not present because of complete dissolution, or present as a biased assemblage, precluding index calculations. Some saddle (xeric C₄ Chloridoideae), bulliform, and larger sedge stem (TWR) phytoliths were observed. Microcharcoal concentrations were very low, suggesting low plant densities and the likely presence of a xeric short-grass savanna in the uplands.

6.5. Zone 5: 2.72 to 2.57 Ma

Zone 5 spans 2.72 Ma (~75 mbs) to 2.57 Ma (5.43 mbs) and occurred during the intensification of NHG. This zone contains the four previously described Barsemoi drainage outcrop diatomites (Deino et al., 2006; Kingston et al., 2007) and other intervals with moderate to high diatom abundance (Westover et al., 2020). There is excellent

phytolith preservation, and pollen (mostly grass) was observed in 11 samples. The first well-preserved phytolith sample occurs at 2.723 Ma (73.66 mbs) coeval with the coldest part of MIS G6 glacial, and there is an increase in microcharcoal concentrations soon after, suggesting an increase in plant density on the landscape. Short-grass/tall-grass savanna dynamics became strongly coupled with insolation at precessional periodicities, with C_4 mesic Panicoideae becoming dominant during insolation maxima and xeric C_4 Chloridoideae becoming dominant during insolation minima (Figs. 3A and 15). Iph values $\leq 27.8\%$ may indicate MAP > 750 mm. This provides evidence that monsoonal precipitation was enhanced by increased insolation enough to change the composition of grasses on the landscape.

In contrast to the previously discussed zones where peaks in June/ July insolation at 30° N appear to correlate with tall-grass savanna dominance, peaks in local insolation during the month that precedes the East African short rains appear to be a better match with tall-grass savanna dominance once NHG intensifies (Fig. 15). Previous studies with good chronological control have indicated that insolation maxima occurring in either March/April or September/October in East Africa may be responsible for enhancement of either the long rains or short rains, respectively (Trauth et al., 2003; Bergner and Trauth, 2004; Verschuren et al., 2009; Junginger et al., 2014). However, age model uncertainty in this part of the BTB13 core is ± 17 kyr, so linking tallgrass savanna dominance to any particular individual insolation curve is difficult. It is interesting to note that the abrupt changes from either short- or tall-grass dominance suggests the existence of an insolation threshold, at which precipitation is significantly enhanced or diminished within 570 years or less. Analysis at a higher resolution than our typical 32-cm intervals may reveal even shorter transition times between humid and arid periods. This nonlinear pattern has similarities to that seen for the onset and termination of the Holocene epoch African Humid Period (Tierney et al., 2011; Armitage et al., 2015; Collins et al.,

Throughout this zone, double peaks in microcharcoal concentrations, separated by ~10 kyr, are associated with peaks in insolation (Fig. 10). Phytoliths from the swamp and stream margin fern Cyclosorus, and trilete spores indicative of ferns suggest the presence of freshwater Cyclosorus-Papyrus swamps or forested streams during the uppermost part of the zone. Pollen and phytoliths from Celtis, a tree associated with a wide variety of mesic habitats, was observed in this zone. This same interval also yielded numerous indicators of afromontane plants such as Podocarpus pollen, increased C3 grass phytoliths, orchid and Murdannia/Floscopa (Commelinaceae)-type phytoliths, and numerous siliceous cysts from chrysophyte golden algae (Figs. 2 and 3). This suggests the possible downward migration of afromontane vegetation from upper elevations and the expansion of swamps during early Pleistocene glacials. However, there is no evidence that woody cover increased above the 40% detection limit of the D/P° phytolith index along the lake margins.

Although the diatom (Westover et al., 2020) and mineralogy (Minkara et al., 2020) datasets indicate extreme hydroclimate variability during the Zone 5 interval (Fig. 3F), it does not appear vegetation was varying to quite the same degree. In fact, there is a decreasing trend in plant compositional turnover across the extent of the BTB13 record (Fig. 8D). The previously discussed abrupt changes between short and tall-grass dominance are significant, but can be induced by a MAP change of a few hundred mm. It is possible that sometime after ~3.10 Ma, subsidence associated with rifting created a balanced-fill and/or underfilled lake-type basin (sensu Carroll and Bohacs, 1999). This new basin configuration could have then become more sensitive to changes in precipitation, a phenomena which has been referred to as an amplifier lake (Trauth et al., 2010). Junginger and Trauth (2013) have shown that relatively small changes in precipitation can result in very large changes in lake depth for paleolake Suguta. Thus, the relative changes in hydroclimate recorded by some paleolimnological and sedimentary proxies may not be proportional to that recorded or

experienced by terrestrial vegetation.

7. Broader implications from this study

The results obtained here have broader implications for phytolith analysis and paleoenvironmental reconstructions from rift valley settings. Phytolith dissolution and morphotype assemblage bias must be determined to ensure robust and accurate interpretation of phytolith indices such as Iph and D/P°. Because the potential for palm phytolith misidentification resulting from the morphological similarity of sponge spherasters is very high, the results of some studies may have to be reconsidered and reinterpreted. An increase in sponge abundance at low elevation rift valley locations likely signals increasing alkalinity/ pH. Phytolith studies from paleosols are likely missing precession-scale variability. Phytolith assemblages from paleosols and lake sediments formed during insolation minima (maxima) will be recording more xeric (mesic) adapted vegetation. And lastly, tree cover reconstructions based on modern calibrations of C₃/C₄ isotopic mixing models need to consider that C3 grasses can be abundant in some low elevation mesophytic and hydrophytic habitats.

8. Conclusions

Millennial-scale phytolith and microcharcoal records from 3.29 to 2.58 Ma track short-and long-term changes in vegetation and fire during the MPWP and the onset and intensification of NHG in the Baringo Basin/Tugen Hills of Kenya. Prior to ~3.04 Ma, landscapes varied between open savanna, woodland, and forest at typically precessional (19-23 kyr) periodicities. During the MPWP, high microcharcoal abundance suggests regional turnover from wooded to open habitats was driven, at least in part, by fire. After ~ 3.04 Ma low elevation woody cover likely never exceeded 40%, and mesic tall-grass and xeric short-grass savanna fluctuated with precessional periodicities. Mesic C4 tall-grass savanna dominated during insolation maxima, and xeric C₄ short-grass savanna dominated during insolation minima. This is a novel observation that likely had an influence on herbivore guild populations, predator-prey relationships, and hominin behavior and landscape use. Comparison of our results with the 30° N to 30° S insolation gradient curve suggests that cross-equatorial advection of heat and moisture may enhance or modulate eastern African precipitation.

With 652 samples analyzed from a 228 m core that spans 730 kyr, this record represents one of the most extensive phytolith studies conducted to date, and illustrates how phytoliths can complement other types of reconstruction datasets. The combined phytolith and pollen data provide the first Pliocene record of plant taxa for the Baringo Basin and Tugen Hills, helping to fill a critical gap in plant functional type data for the central Kenya Rift Valley and its associated hominin localities. This study also fills a gap in orbitally resolved regional vegetation data useful for paleodata—model comparisons for the onset of NHG and the MPWP, the latter of which is often used as an analog for future warming.

Declaration of Competing Interest

The authors declare that they have no known competing financial interests or personal relationships that could have appeared to influence the work reported in this paper.

Acknowledgments

We thank Kaitlynn Walker, Lizbeth Murillo, Murtadha Al Malallah, Sirawitch Nantanoi, and Marie Mathis from the University of Arizona for assisting with the phytolith/microcharcoal and pollen separations. This research was conducted as part of the Hominin Sites and Paleolakes Drilling Program (HSPDP). Initial BTB13 core processing

and sampling was carried out at the National Lacustrine Core Facility (LacCore), University of Minnesota, USA. BTB13 is archived at LacCore. Funding for this work was provided by National Science Foundation (NSF) grants EAR-1123942, BCS-1241859, EAR-1338553, and the International Continental Scientific Drilling Program (ICDP). We thank Doris Barboni, Jay Quade, and Steve Archer for commenting on an early version of this manuscript, special issue guest editors Jenni Scott and Mark Sier, and two anonymous reviewers for comments that greatly improved the manuscript. This is publication #25 of the Hominin Sites and Paleolakes Drilling Project.

Appendix A. Supplementary data

Supplementary data to this article can be found online at https://doi.org/10.1016/j.palaeo.2020.109779.

References

- Agnew, A.D.Q., 2013. Upland Kenya Wild Flowers and Ferns. Nature Kenya, Nairobi. Albert, R.M., Bamford, M.K., Cabanes, D., 2009. Palaeoecological significance of palms at Olduvai Gorge, Tanzania, based on phytolith remains. Quat. Int. 193, 41–48.
- Albert, R.M., Bamford, M.K., Stanistreet, I.G., Stollhofen, H., Rivera-Rondón, C.A., Njau, J.K., Blumenschine, R.J., 2018. River-fed wetland palaeovegetation and palaeoecology at the HWK W site, Bed I, Olduvai Gorge. Rev. Palaeobot. Palynol. 259, 223–241.
- Aleman, J.C., Canal-Subitani, S., Favier, C., Bremond, L., 2014. Influence of the local environment on lacustrine sedimentary phytolith records. Palaeogeogr. Palaeoclimatol. Palaeoecol. 414, 273–283.
- Alexandre, A., Meunier, J.D., Lézine, A.M., Vincens, A., Schwartz, D., 1997. Phytoliths: indicators of grassland dynamics during the late Holocene in intertropical Africa. Palaeogeogr. Palaeoclimatol. Palaeoecol. 136, 213–229.
- Ameka, G.K., Clerk, G.C., Pfeifer, E., Rutishauser, R., 2003. Developmental morphology of Ledermanniella bowlingii (Podostemaceae) from Ghana. Plant Syst. Evol. 237, 165–183.
- Archibald, S., Roy, D.P., van Wilgen, B.W., Scholes, R.J., 2009. What limits fire? An examination of drivers of burnt area in southern Africa. Glob. Chang. Biol. 15, 613–630.
- Armitage, S.J., Bristow, C.S., Drake, N.A., 2015. West African monsoon dynamics inferred from abrupt fluctuations of Lake Mega-Chad. Proc. Natl. Acad. Sci. U. S. A. 112, 8543–8548.
- Arráiz, H., Barboni, D., Ashley, G.M., Mabulla, A., Baquedano, E., Domínguez-Rodrigo, M., 2017. The FLK Zinj paleolandscape: Reconstruction of a 1.84 Ma wooded habitat in the FLK Zinj-AMK-PTK-DS archaeological complex, Middle Bed I (Olduvai Gorge, Tanzania). Palaeogeogr. Palaeoclimatol. Palaeoecol. 488, 9–20.
- Ashley, G.M., Tactikos, J.C., Owen, R.B., 2009. Hominin use of springs and wetlands: paleoclimate and archaeological records from Olduvai Gorge (~1.79–1.74 Ma). Palaeogeogr. Palaeoclimatol. Palaeoecol. 272, 1–16.
- Badaut, D., Risacher, F., 1983. Authigenic smectite on diatom frustules in Bolivian saline lakes. Geochim. Cosmochim. Acta 47, 363–375.
- Balch, D.P., Cohen, A.S., Schnurrenberger, D.W., Haskell, B.J., Valero Garces, B.L., Beck, J.W., Cheng, H., Edwards, R.L., 2005. Ecosystem and paleohydrological response to Quaternary climate change in the Bonneville Basin, Utah. Palaeogeogr. Palaeoclimatol. Palaeoecol. 221, 99–122.
- Banyikwa, F.F., Feoli, E., Zuccarello, V., 1990. Fuzzy set ordination and classification of Serengeti short grasslands, Tanzania. J. Veg. Sci. 1, 97–104.
- Barboni, D., 2014. Vegetation of Northern Tanzania during the Plio-Pleistocene: a synthesis of the paleobotanical evidences from Laetoli, Olduvai, and Peninj hominin sites. Quat. Int. 322–323, 264–276.
- Barboni, D., Bremond, L., 2009. Phytoliths of East African grasses: an assessment of their environmental and taxonomic significance based on floristic data. Rev. Palaeobot. Palynol. 158, 29–41.
- Barboni, D., Bonnefille, R., Alexandre, A., Meunier, J.D., 1999. Phytoliths as paleoenvironmental indicators, West Side Middle Awash Valley, Ethiopia. Palaeogeogr. Palaeoclimatol. Palaeoecol. 152, 87–100.
- Barboni, D., Ashley, G.M., Bourel, B., Arráiz, H., Mazur, J.-C., 2019. Springs, palm groves, and the record of early hominins in Africa. Rev. Palaeobot. Palynol. 266, 23–41.
- Barker, P., Fontes, J.C., Gasse, F., 1994. Experimental dissolution of diatom silica in concentrated salt solutions and implications for paleoenvironmental reconstruction. Limnol. Oceanogr. 39, 99–110.
- Bartoli, F., Wilding, L.P., 1980. Dissolution of biogenic opal as a function of its physical and chemical properties. Soil Sci. Soc. Am. 44, 873–878.
- Beck, J.W., Zhou, W., Li, C., Wu, Z., White, L., Xian, F., Kong, X., An, Z., 2018. A 550,000-year record of East Asian monsoon rainfall from 10 be in losss. Science 360, 877–881.
- Belsky, A.J., 1983. Small-scale pattern in grassland communities in the Serengeti National Park, Tanzania. Vegetatio 55, 141–151.
- Belsky, A.J., 1985. Long-term vegetation monitoring in the Serengeti National Park, Tanzania. J. Appl. Ecol. 22, 449–460.
- Belsky, A.J., 1986. Population and community processes in a mosaic grassland in the Serengeti, Tanzania. J. Ecol. 74, 841–856.
- Bender, R., Tobias, P., Bender, N., 2012. The Savannah hypotheses: origin, reception and impact on paleoanthropology. Hist Philos Life Sci 34, 147–184.

- Benvenuto, M.L., Fernández Honaine, M., Osterrieth, M.L., Morel, E., 2015.

 Differentiation of globular phytoliths in Arecaceae and other monocotyledons: morphological description for paleobotanical application. Turk. J. Bot. 39, 341–353.
- Berger, A., Loutre, M.F., 1991. Insolation values for the climate of the last 10 million years. Quat. Sci. Rev. 10, 297–317.
- Bergner, A.G.N., Trauth, M.H., 2004. Comparison of the hydrological and hydrochemical evolution of Lake Naivasha (Kenya) during three highstands between 175 and 60 kyr BP. Palaeogeogr. Palaeoclimatol. Palaeoecol. 215, 17–36.
- Birks, H.J.B., 2007. Estimating the amount of compositional change in late-Quaternary pollen-stratigraphical data. Veg. Hist. Archaeobotany 16, 197–202.
- Bocksberger, G., Schnitzler, J., Chatelain, C., Daget, P., Janssen, T., Schmidt, M., Thiombiano, A., Zizka, G., Ward, D., 2016. Climate and the distribution of grasses in West Africa. J. Veg. Sci. 27, 306–317.
- Bond, W.J., 2015. Fires in the Cenozoic: a late flowering of flammable ecosystems. Front. Plant Sci. 5, 749.
- Bonnefille, R., 2010. Cenozoic vegetation, climate changes and hominid evolution in tropical Africa. Glob. Planet. Chang. 72, 390–411.
- Bonnefille, R., Riollet, G., 1980. Pollens de savanes d'Afrique orientale., Editions du Centre National de la Recherche Scientifique 140, Paris.
- Bonnefille, R., Potts, R., Chalie, F., Jolly, D., Peyron, O., 2004. High-resolution vegetation and climate change associated with Pliocene *Australopithecus afarensis*. Proc. Natl. Acad. Sci. 101, 12125–12129.
- Boury-Esnault, N., Rützler, K., 1997. Thesaurus of sponge morphology. Smithson. Contrib. Zool. 596, 1–55.
- Bremond, L., Alexandre, A., Hely, C., Guiot, J., 2005a. A phytolith index as a proxy of tree cover density in tropical areas: calibration with Leaf Area Index along a forest—savanna transect in southeastern Cameroon. Glob. Planet. Chang. 45, 277–293.
- Bremond, L., Alexandre, A., Peyron, O., Guiot, J., 2005b. Grass water stress estimated from phytoliths in West Africa. J. Biogeogr. 32, 311–327.
- Bremond, L., Alexandre, A., Wooller, M.J., Hély, C., Williamson, D., Schäfer, P.A., Majule, A., Guiot, J., 2008. Phytolith indices as proxies of grass subfamilies on East African tropical mountains. Glob. Planet. Chang. 61, 209–224.
- Bunn, H.T., Gurtov, A.N., 2014. Prey mortality profiles indicate that Early Pleistocene *Homo* at Olduvai was an ambush predator. Quat. Int. 322-323, 44–53.
- Cabanes, D., Shahack-Gross, R., 2015. Understanding fossil phytolith preservation: the role of partial dissolution in paleoecology and archaeology. PLoS One 10, e0125532.
- Campisano, C.J., Cohen, A.S., Arrowsmith, J.R., Asrat, A., Behrensmeyer, A.K., Brown, E.T., Deino, A.L., Deocampo, D.M., Feibel, C.S., Kingston, J.D., 2017. The Hominin Sites and Paleolakes Drilling Project: high-resolution paleoclimate records from the East African Rift System and their implications for understanding the environmental context of hominin evolution. PaleoAnthropology 1–43.
- Carcaillet, C., Bouvier, M., Frechette, B., Larouche, A.C., Richard, P.J.H., 2001.

 Comparison of pollen-slide and sieving methods in lacustrine charcoal analyses for local and regional fire history. Holocene 11, 467–476.
- Carroll, A.R., Bohacs, K.M., 1999. Stratigraphic classification of ancient lakes: balancing tectonic and climatic controls. Geology 27, 99–102.
- Cohen, A., Campisano, C., Arrowsmith, R., Asrat, A., Behrensmeyer, A.K., Deino, A., Feibel, C., Hill, A., Johnson, R., Kingston, J., Lamb, H., Lowenstein, T., Noren, A., Olago, D., Owen, R.B., Potts, R., Reed, K., Renaut, R., Schäbitz, F., Tiercelin, J.J., Trauth, M.H., Wynn, J., Ivory, S., Brady, K., Apos, Grady, R., Rodysill, J., Githiri, J., Russell, J., Foerster, V., Dommain, R., Rucina, S., Deocampo, D., Russell, J., Billingsley, A., Beck, C., Dorenbeck, G., Dullo, L., Feary, D., Garello, D., Gromig, R., Johnson, T., Junginger, A., Karanja, M., Kimburi, E., Mbuthia, A., McCartney, T., McNulty, E., Muiruri, V., Nambiro, E., Negash, E.W., Njagi, D., Wilson, J.N., Rabideaux, N., Raub, T., Sier, M.J., Smith, P., Urban, J., Warren, M., Yadeta, M., Yost, C., Zinaye, B., 2016. The Hominin Sites and Paleolakes Drilling Project: inferring the environmental context of human evolution from eastern African rift lake deposits. Sci. Drill. 21. 1–16.
- Collins, J.A., Prange, M., Caley, T., Gimeno, L., Beckmann, B., Mulitza, S., Skonieczny, C., Roche, D., Schefuss, E., 2017. Rapid termination of the African Humid Period triggered by northern high-latitude cooling. Nat. Commun. 8, 1372.
- Zhao, F., Collura, L.V., Neumann, K., 2017. Wood and bark phytoliths of West African woody plants. Quatern. Int. 434, 142–159.
- Cuthbert, M.O., Ashley, G.M., 2014. A spring forward for hominin evolution in East Africa. PLoS One 9, e107358.
- Cuthbert, M.O., Gleeson, T., Reynolds, S.C., Bennett, M.R., Newton, A.C., McCormack, C.J., Ashley, G.M., 2017. Modelling the role of groundwater hydro-refugia in East African hominin evolution and dispersal. Nat. Commun. 8, 15696.
- da Costa, F., Klein, D.E., Philbrick, C.T., Bove, C.P., 2018. Silica bodies in leaves of neotropical Podostemaceae: taxonomic and phylogenetic perspectives. Ann. Bot. 122, 1187–1201.
- De Schepper, S., Gibbard, P.L., Salzmann, U., Ehlers, J., 2014. A global synthesis of the marine and terrestrial evidence for glaciation during the Pliocene Epoch. Earth-Sci. Rev. 135, 83–102.
- Deino, A.L., Hill, A., 2002. ⁴⁰Ar/³⁹Ar dating of Chemeron Formation strata encompassing the site of hominid KNM-BC 1, Tugen Hills, Kenya. J. Hum. Evol. 42, 141–151. Deino, A.L., Tauxe, L., Monaghan, M., Hill, A., 2002. ⁴⁰Ar/³⁹Ar geochronology and pa-
- Deino, A.L., Tauxe, L., Monaghan, M., Hill, A., 2002. ⁴⁰Ar/³⁹Ar geochronology and paleomagnetic stratigraphy of the Lukeino and lower Chemeron Formations at Tabarin and Kapcheberek, Tugen Hills, Kenya. J. Hum. Evol. 42, 117–140.
- Deino, A., Kingston, J., Glen, J., Edgar, R., Hill, A., 2006. Precessional forcing of lacustrine sedimentation in the late Cenozoic Chemeron Basin, Central Kenya Rift, and calibration of the Gauss/Matuyama boundary. Earth Planet. Sci. Lett. 247, 41–60.
- Deino, A.L., Sier, M.J., Garello, D.I., Keller, B., Kingston, J.D., Scott, J.J., Dupont-Nivet, G., Cohen, A.S., 2020. Chronostratigraphy of the Baringo-Tugen-Barsemoi (HSPDP-BTB13-1A) core 40Ar/39Ar dating, magnetostratigraphy, tephrostratigraphy, sequence stratigraphy and Bayesian age modeling. In: Scott, J.J., Stone, J.R., Sier, M.J.,

- Kingston, J.D. (Eds.), A High-Resolution, Multi-Proxy Record of Pliocene Hominin Environments in the Kenya Rift Valley: Analysis of the Baringo-Tugen Hills-Barsemoi (BTB) Drill Core. Palaeogeography, Palaeoclimatology, Palaeoecology, this issue.
- deMenocal, P., 1995. Plio-Pleistocene African climate. Science 270, 53-59.
- Deocampo, D.M., Ashley, G.M., 1999. Siliceous islands in a carbonate sea: modern and Pleistocene spring-fed wetlands in Ngorongoro Crater and Oldupai Gorge, Tanzania. J. Sediment. Res. 69, 974–979.
- Derkowski, A., Srodon, J., McCarty, D.K., 2015. Cation exchange capacity and water content of opal in sedimentary basins: example from the Monterey Formation, California. Am. Mineral. 100, 1244–1256.
- Dobson, A., 2009. Food-web structure and ecosystem services: insights from the Serengeti. Philos. Trans. R. Soc. London, Ser. B 364, 1665–1682.
- Dolan, A.M., Haywood, A.M., Hunter, S.J., Tindall, J.C., Dowsett, H.J., Hill, D.J., Pickering, S.J., 2015. Modelling the enigmatic Late Pliocene Glacial Event — Marine Isotope Stage M2. Glob. Planet. Chang. 128, 47–60.
- Edwards, E.J., Osborne, C.P., Stromberg, C.A., Smith, S.A., Consortium, C.G., Bond, W.J., Christin, P.A., Cousins, A.B., Duvall, M.R., Fox, D.L., Freckleton, R.P., Ghannoum, O., Hartwell, J., Huang, Y., Janis, C.M., Keeley, J.E., Kellogg, E.A., Knapp, A.K., Leakey, A.D., Nelson, D.M., Saarela, J.M., Sage, R.F., Sala, O.E., Salamin, N., Still, C.J., Tipple, B., 2010. The origins of C₄ grasslands: integrating evolutionary and ecosystem science. Science 328, 587–591.
- Eichhorn, B., Neumann, K., Garnier, A., 2010. Seed phytoliths in West African Commelinaceae and their potential for palaeoecological studies. Palaeogeogr. Palaeoclimatol. Palaeoecol. 298, 300–310.
- Esteban, I., Vlok, J., Kotina, E.L., Bamford, M.K., Cowling, R.M., Cabanes, D., Albert, R.M., 2017. Phytoliths in plants from the south coast of the Greater Cape Floristic Region (South Africa). Rev. Palaeobot. Palynol. 245, 69–84.
- Faegri, K., Iversen, J., 1989. Textbook of Pollen Analysis, 4th ed. John Wiley and Sons, Chichester, UK.
- Fraysse, F., Pokrovsky, O.S., Schott, J., Meunier, J.-D., 2009. Surface chemistry and reactivity of plant phytoliths in aqueous solutions. Chem. Geol. 258, 197–206.
- Fredlund, G.G., Tieszen, L.T., 1994. Modern phytolith assemblages from the North American Great Plains. J. Biogeogr. 21, 321–335.
- Garnier, A., Neumann, K., Eichhorn, B., Lespez, L., 2012. Phytolith taphonomy in the middle- to late-Holocene fluvial sediments of Ounjougou (Mali, West Africa). Holocene 23, 416–431.
- Hammer, Ø., Harper, D.A.T., Ryan, P.D., 2001. PAST: Paleontological statistics software package for education and data analysis. Palaeontol. Electron. 4, 1–9.
- Hansen, M.C., DeFries, R., Townshend, J.R.G., Carroll, M., Dimiceli, C., Sohlberg, R., 2003. Global percent tree cover at a spatial resolution of 500 meters: first results of the MODIS vegetation continuous fields algorithm. Earth Interact. 7, 1–7.
- Harmand, S., Lewis, J.E., Feibel, C.S., Lepre, C.J., Prat, S., Lenoble, A., Boes, X., Quinn, R.L., Brenet, M., Arroyo, A., Taylor, N., Clement, S., Daver, G., Brugal, J.P., Leakey, L., Mortlock, R.A., Wright, J.D., Lokorodi, S., Kirwa, C., Kent, D.V., Roche, H., 2015. 3.3-million-year-old stone tools from Lomekwi 3, West Turkana, Kenya. Nature 521, 310–315.
- Hay, R.L., 1986. Geologic occurrence of zeolites and some associated minerals. Pure Appl. Chem. 58, 1339–1342.
- Haywood, A.M., Dowsett, H.J., Dolan, A.M., 2016. Integrating geological archives and climate models for the mid-Pliocene warm period. Nat. Commun. 7, 10646.
- Hély, C., Bremond, L., Alleaume, S., Smith, B., Sykes, M.T., Guiot, J., 2006. Sensitivity of African biomes to changes in the pecipitation regime. Glob. Ecol. Biogeogr. 15, 258–270
- Hempson, G.P., Archibald, S., Bond, W.J., 2015a. A continent-wide assessment of the form and intensity of large mammal herbivory in Africa. Science 350, 1056–1061.
- Hempson, G.P., Archibald, S., Bond, W.J., Ellis, R.P., Grant, C.C., Kruger, F.J., Kruger, L.M., Moxley, C., Owen-Smith, N., Peel, M.J., Smit, I.P., Vickers, K.J., 2015b. Ecology of grazing lawns in Africa. Biol. Rev. Camb. Philos. Soc. 90, 979–994.
- Hill, A., 1981. Why study paleoecology? Nature 293, 340.
- Hill, A., 1985. Early hominid from Baringo, Kenya. Nature 315, 222-224.
- Hill, A., 2002. Paleoanthropological research in the Tugen Hills, Kenya. J. Hum. Evol. 42, 1–10.
- Hill, A., Ward, S., Deino, A., Curtis, G., Drake, R., 1992. Earliest Homo. Nature 355, 719–722.
- Huffman, M.A., Gotoh, S., Turner, L.A., Hamai, M., Yoshida, K., 1997. Seasonal trends in intestinal nematode infection and medicinal plant use among chimpanzees in the Mahale Mountains, Tanzania. Primates 38, 111–125.
- Iler, R.K., 1979. The Chemistry of Silica: Solubility, Polymerization, Colloid and Surface Properties, and Biochemistry. John Wiley and Sons, New York.
- Isbell, L.A., 1998. Diet for a small primate: insectivory and gummivory in the (large) patas monkey (*Erythrocebus patas pyrrhonotus*). Am. J. Primatol. 45, 381–398.
- Issaharou-Matchi, I., Barboni, D., Meunier, J.D., Saadou, M., Dussouillez, P., Contoux, C., Zirihi-Guede, N., 2016. Intraspecific biogenic silica variations in the grass species Pennisetum pedicellatum along an evapotranspiration gradient in South Niger. Flora 220, 84–93.
- Ivory, S.J., Early, R., Sax, D.F., Russell, J., 2016. Niche expansion and temperature sensitivity of tropical African montane forests. Glob. Ecol. Biogeogr. 25, 693–703.
- Ivory, S.J., Lezine, A.M., Vincens, A., Cohen, A.S., 2018. Waxing and waning of forests: Late Quaternary biogeography of southeast Africa. Glob. Chang. Biol. 24, 2939–2951.
- Jacobs, B.F., 2002. Estimation of low-latitude paleoclimates using fossil angiosperm leaves: examples from the Miocene Tugen Hills, Kenya. Paleobiology 28, 399–421.
- Jacobs, B.F., 2004. Palaeobotanical studies from tropical Africa: relevance to the evolution of forest, woodland and savannah biomes. Philos. Trans. R. Soc. London, Ser. B 359, 1573–1583.
- Jacobs, B.F., Pan, A.D., Scotese, C.R., 2010. A review of the Cenozoic vegetation history of Africa. In: Werdelin, L., Sanders, W.J. (Eds.), Cenozoic Mammals of Africa. University

- of California Press, Berkeley, pp. 57-72.
- Junginger, A., Trauth, M.H., 2013. Hydrological constraints of paleo-Lake Suguta in the Northern Kenya Rift during the African Humid Period (15–5ka BP). Glob. Planet. Chang. 111, 174–188.
- Junginger, A., Roller, S., Olaka, L.A., Trauth, M.H., 2014. The effects of solar irradiation changes on the migration of the Congo Air Boundary and water levels of paleo-Lake Suguta, Northern Kenya Rift, during the African Humid Period (15–5ka BP). Palaeogeogr. Palaeoclimatol. Palaeoecol. 396, 1–16.
- Kealhofer, L., Piperno, D.R., 1998. Opal phytoliths in southeast Asian flora. Smithson. Contrib. Bot. 88, 1–39.
- Kingston, J.D., 2007. Shifting adaptive landscapes: progress and challenges in reconstructing early hominid environments. Yb. Phys. Anthrop. 50, 20–58.
- Kingston, J.D., Fine Jacobs, B., Hill, A., Deino, A., 2002. Stratigraphy, age and environments of the late Miocene Mpesida Beds, Tugen Hills, Kenya. J. Hum. Evol. 42, 95–116
- Kingston, J.D., Deino, A.L., Edgar, R.K., Hill, A., 2007. Astronomically forced climate change in the Kenyan Rift Valley 2.7-2.55 Ma: implications for the evolution of early hominin ecosystems. J. Hum. Evol. 53, 487–503.
- Koi, S., Ikeda, H., Rutishauser, R., Kato, M., 2015. Historical biogeography of river-weeds (Podostemaceae). Aquat. Bot. 127, 62–69.
- Kutzbach, J.E., Guan, J., He, F., Cohen, A.S., Orland, I.J., Chen, G., 2020. African climate response to orbital and glacial forcing in 140,000-y simulation with implications for early modern human environments. Proc. Natl. Acad. Sci. 117, 2255–2264.
- Laskar, J., Robutel, P., Joutel, F., Gastineau, M., Correia, A.C.M., Levrard, B., 2004. A long-term numerical solution for the insolation quantities of the Earth. Astron. Astrophys. 428, 261–285.
- Lehmann, C.E., Anderson, T.M., Sankaran, M., Higgins, S.I., Archibald, S., Hoffmann, W.A., Hanan, N.P., Williams, R.J., Fensham, R.J., Felfili, J., Hutley, L.B., Ratnam, J., San Jose, J., Montes, R., Franklin, D., Russell-Smith, J., Ryan, C.M., Durigan, G., Hiernaux, P., Haidar, R., Bowman, D.M., Bond, W.J., 2014. Savanna vegetation-fire-climate relationships differ among continents. Science 343, 548–552.
- Levin, M.J., 2019. Prehistoric agricultural transformations in tropical Remote Oceania: towards comprehensive phytolith analysis. Ouat. Int. 529, 75–90.
- Li, R., Fan, J., Vachula, R.S., Tan, S., Qing, X., 2019. Spatial distribution characteristics and environmental significance of phytoliths in surface sediments of Qingshitan Lake in Southwest China. J. Paleolimnol. 61, 201–215.
- Lind, E.M., Morrison, E.S., 1974. East African Vegtation. Longman, London.
- Linder, H.P., 2017. East African Cenozoic vegetation history. Evol. Anthropol. 26, 300–312.
- Lisiecki, L.E., Raymo, M.E., 2005. A Pliocene-Pleistocene stack of 57 globally distributed benthic δ¹⁸O records. Paleoceanography 20, 1–17.
- Lu, H., Liu, K.-B., 2003. Morphological variations of lobate phytoliths from grasses in China and the south-eastern United States. Divers. Distrib. 9, 73–87.
- Łukowiak, M., 2016. Fossil and modern sponge fauna of southern Australia and adjacent regions compared: interpretation, evolutionary and biogeographic significance of the late Eocene 'soft' sponges. Contrib. Zool. 85, 13–35.
- Łukowiak, M., Pisera, A., O'dea, A., 2013. Do spicules in sediments reflect the living sponge community? A test in a Caribbean shallow-water lagoon. Palaios 28, 373–385.
- Lupien, R.L., Russell, J.M., Kingston, J.D., Yost, C.L., Logan, J., Schuh, A., Cohen, A.S., 2020. Vegetation change in the Baringo Basin, East Africa across the onset of Northern Hemisphere Glaciation 3.3–2.6 Ma. In: Scott, J.J., Stone, J.R., Sier, M.J., Kingston, J.D. (Eds.), A High-Resolution, Multi-Proxy Record of Pliocene Hominin Environments in the Kenya Rift Valley: Analysis of the Baringo-Tugen Hills-Barsemoi (BTB) Drill Core. Palaeogeography, Palaeoclimatology, Palaeoecology, this issue.
- Madella, M., Alexandre, A., Ball, T., 2005. International code for phytolith nomenclature 1.0. Ann. Bot. 96, 253–260.
- Maley, J., 1970. Contributions a l'etude du Bassin tchadien Atlas de pollens du Tchad. Bull. Jard. Bot. Natl. Belgique/Bulletin Natl. Plantentuin Belg. 40, 29–48.
- Manconi, R., Pronzato, R., 2009. Atlas of African Freshwater Sponges. Royal Museum for Central Africa, Tervuren.
- Mariner, R.H., Surdam, R.C., 1970. Alkalinity and formation of zeolites in saline alkaline lakes. Science 170, 977–980.
- McNaughton, S.J., 1983. Serengeti grassland ecology: the role of composite environmental factors and contingency in community organization. Ecol. Monogr. 53, 291–320.
- McNaughton, S.J., 1985. Ecology of a grazing ecosystem: the Serengeti. Ecol. Monogr. 55, 259–294
- Michalopoulos, P., Aller, R.C., 2004. Early diagenesis of biogenic silica in the Amazon delta: alteration, authigenic clay formation, and storage. Geochim. Cosmochim. Acta 68, 1061–1085.
- Michalopoulos, P., Aller, R.C., Reeder, R.J., 2000. Conversion of diatoms to clays during early diagenesis in tropical, continental shelf muds. Geology 28, 1095–1098.
- Minkara, K.E., Deocampo, D.M., Rabideaux, N.M., Kingston, J.D., Deino, A.L., Cohen, A.S., Campisano, C.J., 2020. Zeolite facies and implications for environmental change from the Chemeron Formation of the Baringo Basin, Kenya Rift, 3.3–2.6 Ma. In: Scott, J.J., Stone, J.R., Sier, M.J., Kingston, J.D. (Eds.), A High-Resolution, Multi-Proxy Record of Pliocene Hominin Environments in the Kenya Rift Valley: Analysis of the Baringo-Tugen Hills-Barsemoi (BTB) Drill Core. Palaeogeography, Palaeocclimatology, Palaeoecology, this issue.
- Mitani, M., Amagiw, J.Y., Antoine Oko, R., Moutsambote, J.-M., Yumoto, T., Maruhashi, T., 1993. Approaches in density estimates and reconstruction of social groups in a western lowland gorilla population in the Ndoki Forest, Northern Congo. Tropics 2, 219–229.
- Müller, J., Sieglstetter, R., Jäger-Zürn, I., 2003. First record of Podostemaceae in Benin with remarks on the ecology of *Tristicha trifaria* (Tristichoideae) in Benin and Burkina faso. Belg. J. Bot. 136. 52–58.

- Neumann, K., Fahmy, A.G., Muller-Scheessel, N., Schmidt, M., 2017. Taxonomic, ecological and palaeoecological significance of leaf phytoliths in West African grasses. Ouat. Int. 434, 15–32.
- Ngaira, J.K., 2005. Implications of climate change on the management of Rift Vally lakes in Kenya: the case of Lake Baringo. In: Odada, E.O., Olago, D., Ochola, W., Ntiba, M., Wandiga, S., Gichuki, N., Oyieke, H. (Eds.), Proceedings of the 11th World Lakes Conference. Nairobi, Kenya, pp. 133–138.
- Novello, A., Barboni, D., Berti-Equille, L., Mazur, J.-C., Poilecot, P., Vignaud, P., 2012. Phytolith signal of aquatic plants and soils in Chad, Central Africa. Rev. Palaeobot. Palynol. 178, 43–58.
- Novello, A., Lebatard, A.-E., Moussa, A., Barboni, D., Sylvestre, F., Bourlès, D.L., Paillès, C., Buchet, G., Decarreau, A., Duringer, P., Ghienne, J.-F., Maley, J., Mazur, J.-C., Roquin, C., Schuster, M., Vignaud, P., 2015. Diatom, phytolith, and pollen records from a 10Be/9Be dated lacustrine succession in the Chad basin: insight on the Miocene–Pliocene paleoenvironmental changes in Central Africa. Palaeogeogr. Palaeoclimatol. Palaeoecol. 430, 85–103.
- Novello, A., Barboni, D., Sylvestre, F., Lebatard, A.E., Pailles, C., Bourles, D.L., Likius, A., Mackaye, H.T., Vignaud, P., Brunet, M., 2017. Phytoliths indicate significant arboreal cover at *Sahelanthropus* type locality TM266 in northern Chad and a decrease in later sites. J. Hum. Evol. 106, 66–83.
- Ollendorf, A.L., 1992. Toward a classification scheme of sedge (Cyperaceae) phytoliths. In: Rapp, G.R., Mulholland, S.C. (Eds.), Phytolith Systematics: Emerging Issues. Plenum, New York, pp. 91–111.
- Owen, R.B., Muiruri, V.M., Lowenstein, T.K., Renaut, R.W., Rabideaux, N., Luo, S., Deino, A.L., Sier, M.J., Dupont-Nivet, G., McNulty, E.P., Leet, K., Cohen, A., Campisano, C., Deocampo, D., Shen, C.C., Billingsley, A., Mbuthia, A., 2018. Progressive aridification in East Africa over the last half million years and implications for human evolution. Proc. Natl. Acad. Sci. 115, 11174–11179.
- Pays, O., Blanchard, P., Valeix, M., Chamaille-Jammes, S., Duncan, P., Periquet, S., 2012. Detecting predators and locating competitors while foraging: an experimental study of a medium-sized herbivore in an African savanna. Oecologia 169, 419–430.
- Pickford, M., Johanson, D.C., Lovejoy, C.O., White, T.D., Aronson, J.L., 1983. A hominoid humeral fragment from the Pliocene of Kenya. Am. J. Phys. Anthropol. 60, 337–346.
- Piperno, D.R., 2006. Phytoliths: A Comprehensive Guide for Archaeologists and Paleoecologists. AltaMira Press, Lanham, MD.
- Piperno, D.R., Pearsall, D.M., 1998. The silica bodies of tropical American grasses: morphology, taxonomy, and implications for grass systematics and fossil phytolith identification. Smithson. Contrib. Bot. 85, 1–40.
- Potts, R., 1998. Environmental hypothesis of hominin evolution. Am. J. Phys. Anthropol. 41, 93–136.
- Potts, R., 2004. Paleoenvironmental basis of cognitive evolution in great apes. Am. J. Primatol. 62, 209–228.
- Prell, W.L., Kutzbach, J., 1987. Monsoon variability over the past 150,000 years. J. Geophys. Res. 92, 8411–8425.
- Prentice, A.J., Webb, E.A., 2016. The effect of progressive dissolution on the oxygen and silicon isotope composition of opal-A phytoliths: Implications for palaeoenvironmental reconstruction. Palaeoeogr. Palaeoclimatol. Palaeoecol. 453, 42–51.
- Prescott, C.L., Haywood, A.M., Dolan, A.M., Hunter, S.J., Pope, J.O., Pickering, S.J., 2014.
 Assessing orbitally-forced interglacial climate variability during the mid-Pliocene
 Warm Period. Earth Planet. Sci. Lett. 400, 261–271.
- Prychid, C.J., Rudall, P.J., Gregory, M., 2003. Systematics and biology of silica bodies in monocotyledons. Bot. Rev. 69, 377–440.
- Quigley, K.M., Anderson, T.M., 2014. Leaf silica concentration in Serengeti grasses increases with watering but not clipping: insights from a common garden study and literature review. Front. Plant Sci. 5, 568.
- R Core Team, 2018. R: A Language and Environment for Statistical Computing. R
- Foundation for Statistical Computing, Vienna, Austria. https://www.R-project.org/. Renaut, R., 1993. Zeolitic diagenesis of late Quaternary fluviolacustrine sediments and associated calcrete formation in the Lake Bogoria Basin, Kenya Rift Valley. Sedimentology 40, 271–301.
- Renaut, R.W., Jones, B., Tiercelin, J.J., Tarits, C., 2002. Sublacustrine precipitation of hydrothermal silica in rift lakes: evidence from Lake Baringo, central Kenya Rift Valley. Sediment. Geol. 148, 235–257.
- Rosen, A.M., 1992. Preliminary identification of silica skeletons from Near Eastern archaeological sites: an anatomical approach. In: George Rapp, J., Mulholland, S.C. (Eds.), Phytolith Systematics: Emerging Issues. Plenum, New York, pp. 129–147.
- Runge, F., 1999. The opal phytolith inventory of soils in central Africa —quantities, shapes, classification, and spectra. Rev. Palaeobot. Palynol. 107, 23–53.
- Salzmann, U., Haywood, A.M., Lunt, D.J., Valdes, P.J., Hill, D.J., 2008. A new global biome reconstruction and data-model comparison for the Middle Pliocene. Glob. Ecol. Biogeogr. 17, 432–447.
- Salzmann, U., Haywood, A.M., Lunt, D.J., 2009. The past is a guide to the future? Comparing Middle Pliocene vegetation with predicted biome distributions for the twenty-first century. Philos. Trans. A Math Phys. Eng. Sci. 367, 189–204.
- Salzmann, U., Williams, M., Haywood, A.M., Johnson, A.L.A., Kender, S., Zalasiewicz, J., 2011. Climate and environment of a Pliocene warm world. Palaeogeogr. Palaeoclimatol. Palaeoecol. 309, 1–8.
- Schulz, M., Mudelsee, M., 2002. REDFIT: estimating red-noise spectra directly from unevenly spaced paleoclimatic time series. Comput. Geosci. 28, 421–426.
- Scott, J.J., Chupik, D.T., Deino, A.L., Stockhecke, M., Kingston, J.D., Westover, K.S., Lukens, W.E., Deocampo, D.M., Yost, C.L., Billingsley, A.L., Minkara, K.E., Ortiz, K., Cohen, A.S., 2020. Sequence stratigraphic framework for lacustrine transgression-regression cycles in the 3.3–2.6 Ma interval of the Chemeron Formation BTB13 core, Baringo Basin, Kenya Rift Valley. In: Scott, J.J., Stone, J.R., Sier, M.J., Kingston, J.D. (Eds.), A High-Resolution, Multi-Proxy Record of Pliocene Hominin Environments in the Kenya Rift Valley: Analysis of the Baringo-Tugen Hills-Barsemoi (BTB) Drill Core.

- Palaeogeography, Palaeoclimatology, Palaeoecology, this issue.
- Scurfield, G., Anderson, C.A., Segnit, E.R., 1974. Silica in woody plants. Aust. J. Bot. 22, 211–229
- Simpson, K.J., Ripley, B.S., Christin, P.A., Belcher, C.M., Lehmann, C.E., Thomas, G.H., Osborne, C.P., 2016. Determinants of flammability in savanna grass species. J. Ecol. 104, 138–148.
- Stewart, K.M., 2009. Fossil fish from the Nile River and its southern basins. In: Dumont, H.J. (Ed.), The Nile: Origin, Environments, Limnology and Human Use. Springer, Dordrecht, pp. 676–704.
- Strömberg, C.A.E., 2009. Methodological concerns for analysis of phytolith assemblages: does count size matter? Quat. Int. 193, 124–140.
- Strömberg, C.A.E., Dunn, R.E., Crifò, C., Harris, E.B., 2018. Phytoliths in paleoecology: analytical considerations, current use, and future directions. In: Croft, D., Su, D., Simpson, S. (Eds.), Methods in Paleoecology. Springer, Cham, Switzerland, pp. 235–287.
- Tan, N., Ramstein, G., Dumas, C., Contoux, C., Ladant, J.-B., Sepulchre, P., Zhang, Z., De Schepper, S., 2017. Exploring the MIS M2 glaciation occurring during a warm and high atmospheric CO₂ Pliocene background climate. Earth Planet. Sci. Lett. 472, 266–276.
- Taub, D.R., 2000. Climate and the U.S. distribution of C_4 grass subfamilies and decarboxylation variants of C_4 photosynthesis. Am. J. Bot. 87, 1211–1215.
- ter Braak, C.J.F., 1986. Canonical correspondence analysis: a new eigenvector technique for multivariate direct gradient analysis. Ecology 67, 1167–1179.
- Tierney, J.E., Lewis, S.C., Cook, B.I., LeGrande, A.N., Schmidt, G.A., 2011. Model, proxy and isotopic perspectives on the East African Humid Period. Earth Planet. Sci. Lett. 307, 103–112.
- Trauth, M.H., Deino, A.L., Bergner, A.G.N., Strecker, M.R., 2003. East African climate change and orbital forcing during the last 175 kyr BP. Earth Planet. Sci. Lett. 206, 297–313.
- Trauth, M.H., Maslin, M.A., Deino, A.L., Junginger, A., Lesoloyia, M., Odada, E.O., Olago, D.O., Olaka, L.A., Strecker, M.R., Tiedemann, R., 2010. Human evolution in a variable environment: the amplifier lakes of Eastern Africa. Quat. Sci. Rev. 29, 2981–2988.
- Tuenter, E., Weber, S.L., Hilgen, F.J., Lourens, L.J., 2003. The response of the African summer monsoon to remote and local forcing due to precession and obliquity. Glob. Planet. Chang. 36, 219–235.
- Turner, R., Kelly, A., Roberts, N., 2008. A critical assessment and experimental comparison of microscopic charcoal extraction methods. In: Fiorentino, G., Margi, D. (Eds.), Charcoals from the Past: Cultural and Palaeoenvironmental Implications. Archaeopress, Oxford, pp. 225–272.
- Vacelet, J., Tiercelin, J.J., Gasse, F., 1991. The sponge Dosilia brouni (Spongillidae) in Lake Baringo, Gregory Rift, Kenya. Hydrobiologia 211, 11–18.
- van Breugel, P., Kindt, R., Lillesø, J.P.B., Bingham, M., Demissew, S., Dudley, C., Friis, I., Gachathi, F., Kalema, J., Mbago, F., Moshi, H.N., Mulumba, J., Namaganda, M., Ndangalasi, H.J., Ruffo, C.K., Védaste, M., Jamnadass, R., Graudal, L., 2015. Potential Natural Vegetation Map of Eastern Africa (Burundi, Ethiopia, Kenya, Malawi, Rwanda, Tanzania, Uganda and Zambia). Version 2.0. Forest & Landscape Denmark and World Agroforestry Centre (ICRAF) URL: http://vegetationmap4africa.org.
- Van Cappellen, P., Dixit, S., van Beusekom, J., 2002. Biogenic silica dissolution in the oceans: Reconciling experimental and field-based dissolution rates. Glob. Biogeochem. Cycles 16 23-21–23-10.
- van Wyk, J., 1979. A general account of the grass cover of Africa. In: Numata, M. (Ed.), Ecology of Grasslands and Bamboolands of the World. Junk BV Publishers, The Hague, pp. 124–132.
- Verschuren, D., Sinninghe Damste, J.S., Moernaut, J., Kristen, I., Blaauw, M., Fagot, M., Haug, G.H., members, C.p, 2009. Half-precessional dynamics of monsoon rainfall near the East African Equator. Nature 462, 637–641.
- Vincens, A., Lézine, A.M., Buchet, G., Lewden, D., Le Thomas, A., 2007. African pollen database inventory of tree and shrub pollen types. Rev. Palaeobot. Palynol. 145, 135–141.
- Wallis, L., 2003. An overview of leaf phytolith production patterns in selected northwest Australian flora. Rev. Palaeobot. Palynol. 125, 201–248.
- Wells, J.C., Stock, J.T., 2007. The biology of the colonizing ape. Am. J. Phys. Anthropol. Suppl 45, 191–222.
- Westover, K.S., Stone, J.R., Yost, C.L., Scott, J.J., Cohen, A.S., Rabideaux, N.M., Stockhecke, M., Kingston, J.D., 2020. Diatom paleolimnology of late Pliocene Barringo Basin (Kenya) paleolakes. In: Scott, J.J., Stone, J.R., Sier, M.J., Kingston, J.D. (Eds.), A High-Resolution, Multi-Proxy Record of Pliocene Hominin Environments in the Kenya Rift Valley: Analysis of the Baringo-Tugen Hills-Barsemoi (BTB) Drill Core. Palaeogeography, Palaeoclimatology, Palaeoecology, https://doi.org/10.1016/j. palaeo.2019.109382. this issue.
- White, F., 1983. The Vegetation of Africa. A Descriptive Memoir to Accompany the UNESCO/AETFAT/UNSO Vegetation Map of Africa. UNESCO, Paris, France.
- Williams, E.V., Elia Ntandu, J., Ficinski, P., Vorontsova, M., 2016. Checklist of serengeti ecosystem grasses. Biodivers. Data J. 4, e8286.
- Yost, C.L., Blinnikov, M.S., 2011. Locally diagnostic phytoliths of wild rice (Zizania palustris L.) from Minnesota, USA: comparison to other wetland grasses and usefulness for archaeobotany and paleoecological reconstructions. J. Archaeol. Sci. 38, 1977–1991.
- Yost, C.L., Blinnikov, M.S., Julius, M.L., 2013. Detecting ancient wild rice (*Zizania* spp. L.) using phytoliths: a taphonomic study of modern wild rice in Minnesota (USA) lake sediments. J. Paleolimnol. 49, 221–236.
- Yost, C.L., Jackson, L.J., Stone, J.R., Cohen, A.S., 2018. Subdecadal phytolith and charcoal records from Lake Malawi, East Africa imply minimal effects on human evolution from the ~74 ka Toba supereruption. J. Hum. Evol. 116, 75–94.